

The Ventilated Ocean

PATRICK HAERTEL AND ALEXEY FEDOROV

Geology and Geophysics, Yale University, New Haven, Connecticut

(Manuscript received 22 September 2010, in final form 27 July 2011)

ABSTRACT

Adiabatic theories of ocean circulation and density structure have a long tradition, from the concept of the ventilated thermocline to the notion that deep ocean ventilation is controlled by westerly winds over the Southern Ocean. This study explores these ideas using a recently developed Lagrangian ocean model (LOM), which simulates ocean motions by computing trajectories of water parcels. A unique feature of the LOM is its capacity to model ocean circulations in the adiabatic limit, in which water parcels exactly conserve their densities when they are not in contact with the ocean surface. The authors take advantage of this property of the LOM and consider the circulation and stratification that develop in an ocean with a fully adiabatic interior (with both isopycnal and diapycnal diffusivities set to zero). The ocean basin in the study mimics that of the Atlantic Ocean and includes a circumpolar channel. The model is forced by zonal wind stress and a density restoring at the surface.

Despite the idealized geometry, the relatively coarse model resolution, and the lack of atmospheric coupling, the nondiffusive ocean maintains a density structure and meridional overturning that are broadly in line with those observed in the Atlantic Ocean. These are generated by just a handful of key water pathways, including shallow tropical cells described by ventilated thermocline theory; a deep overturning cell in which sinking North Atlantic Deep Water eventually upwells in the Southern Ocean before returning northward as Antarctic Intermediate Water; a Deacon cell that results from a topographically steered and corkscrewing circumpolar current; and weakly overturning Antarctic Bottom Water, which is effectively ventilated only in the Southern Hemisphere.

The main conclusion of this study is that the adiabatic limit for the ocean interior provides the leading-order solution for ocean overturning and density structure, with tracer diffusion contributing first-order perturbations. Comparing nondiffusive and diffusive experiments helps to quantify the changes in stratification and circulation that result from adding a moderate amount of tracer diffusion in the ocean model, and these include an increase in the amplitude of the deep meridional overturning cell of several Sverdrups, a 10%–20% increase in Northern Hemispheric northward heat transport, a stronger stratification just below the main thermocline, and a more realistic bottom overturning cell.

1. Introduction

For more than 70 years oceanographers have been aware that vertical variations in density in the oceans could result from adiabatic transports along isopycnal surfaces of water masses formed at different latitudes (Pedlosky 1996). Montgomery (1938) and Iselin (1939) were the first to introduce such a concept of thermocline ventilation. Welander (1959) proposed the first adiabatic thermocline model based on ideal-fluid equations. The adiabatic framework was further discussed by Veronis (1969). Luyten Pedlosky and Stommel (1983) and Huang

(1988) formalized this idea into a rigorous adiabatic theory for the density and flow structure of the upper ocean. These ventilated thermocline theories, however, are incomplete in that they require a background stratification, which is typically defined at the eastern boundary of the ocean basin. Traditionally, it has been thought that deep ocean thermal structure—and hence the background stratification needed for adiabatic theories—is determined by a balance between vertical advection and vertical diffusion of heat (e.g., Robinson and Stommel 1959). In fact, numerous studies of ocean thermohaline circulation in closed basins invoke this balance as a driving mechanism for the deep ocean circulation (e.g., Bryan 1987; Huang 1999; Park and Bryan 2000; Fedorov et al. 2007).

The tension between adiabatic and diabatic ways of thinking about ocean stratification and circulation is

Corresponding author address: Dr. Patrick T. Haertel, Geology and Geophysics, Yale University, 210 Whitney Ave., New Haven, CT 06510.
E-mail: patrick.haertel@yale.edu

reflected in recent studies of ocean thermal structure (Tziperman 1986; Samelson and Vallis 1997; Samelson 2004; Boccaletti et al. 2004; Fedorov et al. 2010), ocean energetics (Wunsch and Ferrari 2004), responses to freshwater fluxes (e.g., Barreiro et al. 2008; Fedorov et al. 2004), and different observations of ocean vertical mixing (Ledwell et al. 1993; Polzin et al. 1997). Moreover, the work of Toggweiler and Samuels (1995, 1998) and subsequent studies (e.g., Gnanadesikan 1999; Gnanadesikan and Hallberg 2000; Bryden and Cunningham 2003) point to the important role of Southern Ocean processes such as wind-driven upwelling and eddy fluxes in maintaining the global ocean density structure and deep ocean overturning. Most recently, these ideas have been explored in global ocean models (Saenko 2007; Kuhlbrodt et al. 2007), idealized eddy-resolving models of the Atlantic (Wolfe and Cessi 2010), and zonally averaged ocean models (Sevellec and Fedorov 2011).

While it is likely that ocean stratification and circulation are determined by a combination of all aforementioned processes, the question arises whether oceanic meridional overturning and density structure can be maintained even in the complete absence of interior tracer diffusion. The major goal of our study is to address this important question. We use a recently developed Lagrangian ocean model (LOM) (Haertel and Randall 2002; Haertel et al. 2004, 2009; Van Roekel et al. 2009) to examine the effects of completely removing interior tracer diffusion (both diapycnal and isopycnal) on ocean meridional overturning and stratification. We employ an idealized basin with sloping boundaries that includes an extended periodic channel, which captures the gross geometry of the Atlantic Ocean and the Antarctic circumpolar channel.

Our study is in the spirit of Toggweiler and Samuels (1995), and especially Toggweiler and Samuels (1998), who considered ocean stratification and meridional overturning as tracer mixing approached zero. Their modeling results were obtained within a traditional z -coordinate model and were subject to an uncertain amount of spurious numerical mixing (Griffies et al. 2000), as well as explicit horizontal and low vertical diffusion. Here, we actually conduct a simulation in the fully adiabatic limit, albeit for a more idealized setting. We exploit a unique capability of the LOM: the capacity to conduct runs with a tracer diffusivity set to zero, with water parcels exactly conserving their densities in the ocean interior. We also take advantage of the fact that the LOM provides trajectories for every water parcel in the ocean and examine these to determine locations where water masses form, where sinking water ultimately upwells, and how the zonally integrated meridional overturning streamfunction is partitioned into cross-hemispheric and Southern Hemispheric components. Finally, we repeat our simulation with a moderate amount

of tracer diffusion so that we can precisely quantify its contributions to stratification and circulation for our idealized ocean.

The model that we use (the LOM) has several key differences from traditional isopycnal models. First, the LOM has no spurious numerical isopycnal diffusion associated with advection, which means there is no numerical degradation of tracer distributions and the modeler has explicit control over the amount of isopycnal mixing. This feature can be quite useful for simulating both dynamical and biogeochemical tracer distributions, and it is especially important for the long time scales needed for adjustment of the deep ocean. Second, the behavior at the smallest resolvable scales is also unique in the LOM, with spontaneous generation of bolus transports (see section 3e). In addition, unlike isopycnal models, the LOM does not require diffusion of isopycnal layer thicknesses for numerical stability. Finally, the LOM's convective parameterization allows for a convective redistribution of water mass in the vertical that does not involve mixing. In other words, the convective scheme can represent plumes that are completely nonentraining. Because of these model properties we expect adiabatic LOM simulations to show some key differences from isopycnal simulations with no vertical mixing.

This paper is organized as follows. Section 2 outlines the design of our modeling experiments. In section 3 we examine the circulation and density structure of an idealized ocean in the zero-diffusivity (adiabatic) limit and then consider how the presence of tracer diffusion alters stratification, overturning, and key water pathways. Section 4 is a summary and discussion. Details of the LOM and results of several sensitivity tests are provided in the appendix.

2. Experimental design

We carry out a series of modeling experiments that examine to what extent surface forcing and adiabatic ocean circulations alone determine the gross stratification and meridional overturning of an idealized ocean. The experiments take advantage of the Lagrangian formulation of our ocean model (discussed in the appendix), both in terms of its ability to simulate circulations with zero tracer diffusion and its capacity to track every mass element in the ocean. This section describes the idealized ocean, surface forcing, and spinup procedure for the simulations discussed in the remainder of the paper.

a. Idealized ocean

The basin geometry for the idealized ocean is illustrated in Fig. 1. The model domain extends from 70°S to 70°N, and there is a periodic channel that runs along the southern boundary. The maximum depth of the ocean is

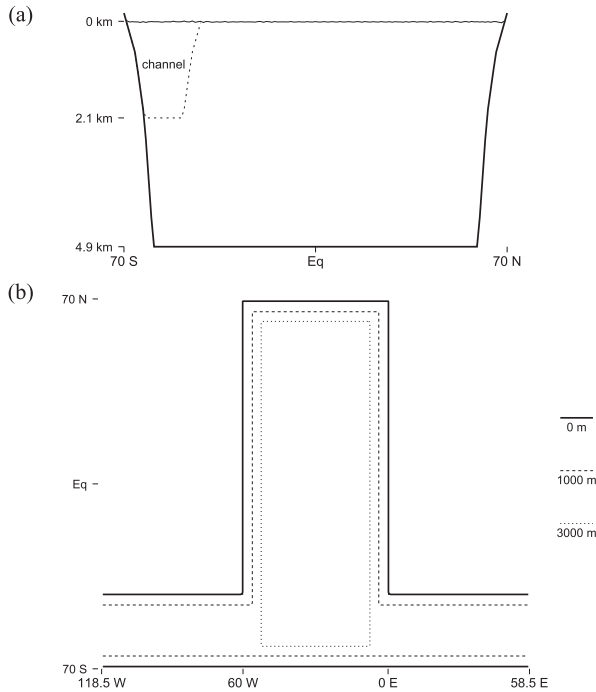


FIG. 1. Basin geometry: (a) north-south vertical cross section and (b) horizontal (view from above). Note that the basin has sloping boundaries on all sides as shown by the dotted and dashed lines in (b).

4.9 km, and the channel is 2.1 km deep. In most of the domain the ocean is about 60° longitude wide, but we make the channel much wider (177° longitude) to create a large region where water can upwell along the southern boundary, which makes the meridional overturning streamfunction more like that of the World Ocean (see below). Because we use a Mercator projection, the actual length of our channel is roughly the same as that of the Antarctic “Circumpolar Channel.” The geometry of the setting resembles that of Wolfe and Cessi (2009, 2010), with several differences: our basin has sloping boundaries, the circumpolar channel is significantly longer, and the depth of basin is almost 5 km (twice that of the previous studies).

For our featured experiments, we represent this ocean as a collection of rather large water parcels with a 3° radius in latitude and longitude and a vertical thickness of about 78 m. Sensitivity tests show that our key results are relatively insensitive to a factor of 2 changes in the horizontal and vertical resolutions of the model (see the appendix). We use a time step of 12 000 s, which is facilitated by using a form of gravity wave retardation (Jensen 1996) to slow external gravity waves by roughly a factor of 10 (see appendix). During the spinup simulation and for supplemental simulations mass elements in the middle and bottom of the ocean are moved in groups of two and four,

respectively, for computational efficiency. This approach is equivalent to using a lower vertical resolution in these regions: it was first used by Haertel et al. (2009).

No horizontal mixing of tracers is used, but we have found that even at low resolution the model generates a bolus transport of isopycnal layer thickness similar to that which a Gent and McWilliams (1990, hereafter GM) parameterization would produce. This important property of the LOM is discussed further in section 3e.

b. Surface forcing

The surface forcings that we apply to the idealized ocean are depicted in Fig. 2. The zonal wind stress (Fig. 2a) is an analytical approximation of the observed wind stress over the Atlantic. However, despite the fact that observed westerlies are stronger in the Southern Hemisphere than in the Northern Hemisphere, we use a symmetric wind forcing so that the primary asymmetry about the equator in our model comes from including the periodic channel. Surface density is restored to a piecewise linear function (Fig. 2b, black line) in most of the model domain. If density is converted to temperature, the surface restoring equates to a 50 W m⁻² °C⁻¹ heat flux, or a piston velocity (Griffies et al. 2009) of about 1 m day⁻¹. The minimum and maximum density for the restoring function are chosen so that simulated surface density fields span the same range as the observed surface density field in the vicinity of 30°W (note that the simulated equatorial density is significantly less than the value of the restoring density there due to equatorial upwelling).

In the version of the LOM used in this study, effects of temperature and salinity on density are not separated. In other words, the LOM prognostic tracer equation is for density itself (see the appendix), which is a corollary of temperature and salinity equations and a linear equation of state for seawater. Consequently, we use the terms pycnocline and thermocline and ocean density and thermal structure interchangeably throughout the paper. Note also that compressibility effects are not included in our model, so it is appropriate to compare the density fields that we plot to observations of potential or neutral density. We include a small region with a higher restoring density near the southern boundary (Fig. 2c) to generate a localized region where deep convection occurs. This feature is included because oceanic deep convection is localized in nature; its impacts are discussed in section 3g. In preliminary experiments we also included a similar perturbation to the restoring density in the north, but found that it had little effect on either stratification or overturning.

c. Spinup procedure and simulation characteristics

In addition to the featured simulation of an ocean with zero diffusivity, we carry out several additional model

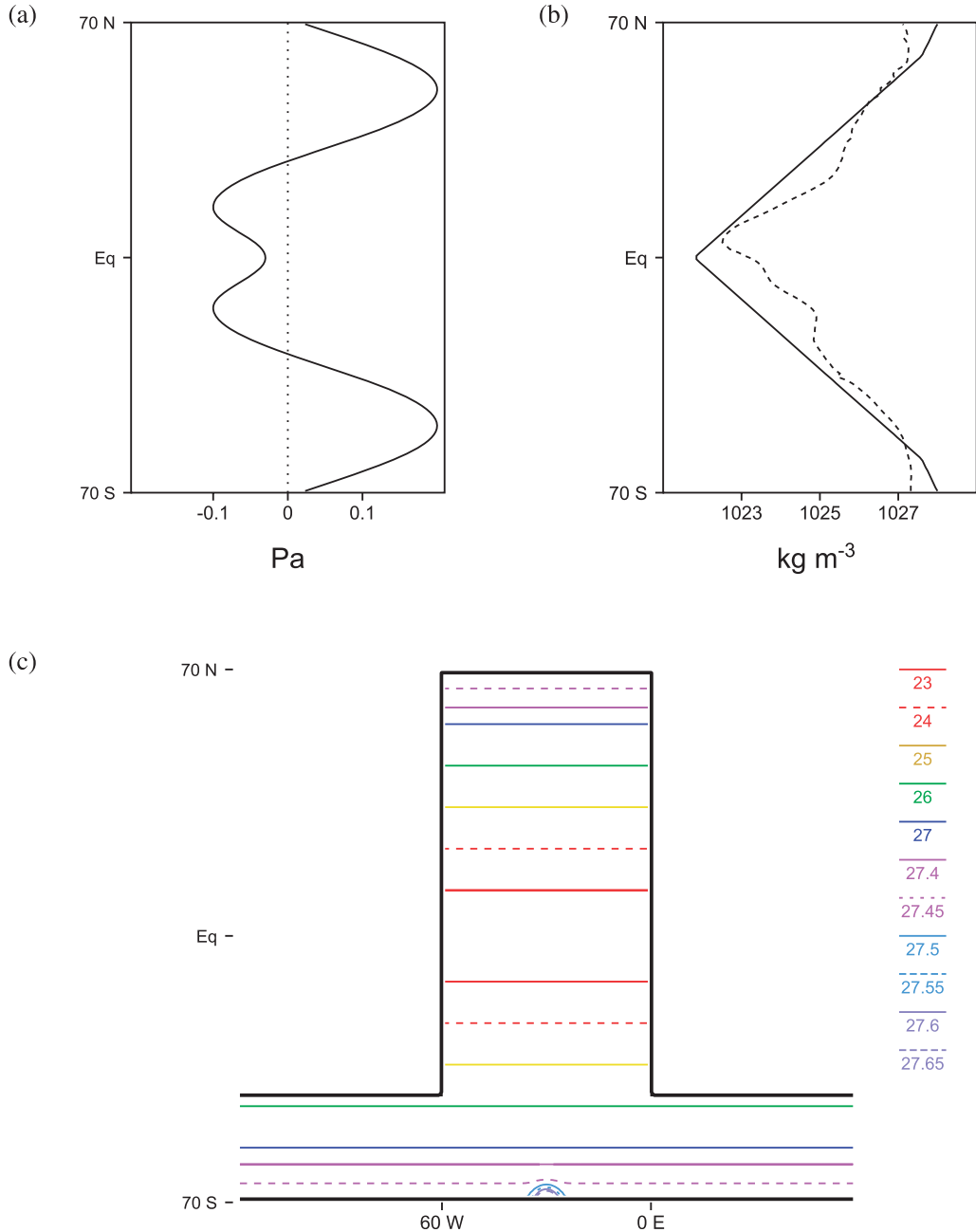


FIG. 2. Surface forcing: (a) zonal wind stress and (b),(c) restoring density. For restoring density we use a zonally uniform profile shown as a solid line in (b) but modified near the southern boundary to include a localized source of dense water at about 70°S, 30°W, evident in (c). Observed surface density along 30°W is shown with a dashed line in (b).

runs aimed at exploring the sensitivities of our solutions. Most of these simulations start with the same initial spinup in which the surface forcing, shown in Fig. 2, is applied to an ocean that has a constant density of 1027 kg m^{-3} . This is a somewhat arbitrary choice for an initial density, but our preliminary experiments (not shown) suggest that the

quasi-steady circulations that ultimately develop are not sensitive to the initial density, provided that it is less than that of parcels sinking in deep convecting regions near the poles. If the initial density is greater than the maximum density of the restoring function, bottom water remains unventilated in the nondiffusive case.

Note that the initial stratification develops as a result of nonentraining convective plumes parameterized via the convective parameterization Lagrangian overturning (LO), which is described in the appendix. That is, in locations where the surface restoring density generates higher densities than the initial condition, vertical position swaps of parcels associated with LO cause relatively dense parcels to descend. This is a physical process; in nature convective plumes transport relatively dense water downward. Although there is mixing in these plumes in nature, it is a matter of debate as to how much mixing. Our representation of convection corresponds to the zero entrainment end of the spectrum, which seems appropriate for a simulation of a nondiffusive ocean.

For the first 3000 years the model is run in its most computationally efficient manner, which means parcels divide (merge) when they enter a region of higher (lower) vertical resolution. After 3000 years of spinup the circulation and density fields are nearly in a statistically steady state: the only nonsteady aspect of time-averaged fields is a very weak increase in the density of the abyss with time ($<0.01 \text{ kg m}^{-3}$ per 1000 yr) that is decreasing in amplitude with time. It is important to note that, whereas diffusivity is set to zero in the main experiment, nonzero vertical and horizontal viscosities are included (10^{-3} and $7 \times 10^4 \text{ m}^2 \text{ s}^{-1}$ respectively), which allows for energy dissipation in the system and corresponds to an infinite Prandtl number.

1) FEATURED SIMULATION: AN OCEAN WITH ZERO DIFFUSIVITY

For the featured simulation, after 3000 years of spinup we discontinue the dividing and merging of parcels and run the simulation out 1000 years longer, without any other modifications in model parameters. We make this change because the occasional merging of parcels used in the spinup generates a very small amount of tracer diffusion, and we are interested in exploring the adiabatic limit (i.e., in having a tracer diffusion of exactly zero) in this study. When no merging of parcels is used, a water parcel's density is exactly conserved when it is not in contact with the surface layer.

For example, Fig. 3 shows the latitude, depth, and density of a water parcel during the last 70 years of the nondiffusive simulation. Each curve is drawn as a solid line for time segments in which the parcel has no contact with the surface. During these segments there is absolutely no change in density; that is, there are no commands in the model code (other than surface forcing) that alter the double-precision variable that represents the parcel's density, which is also confirmed by inspection of model output files. Note that, although one of these periods is a deep and long trip through the deep western

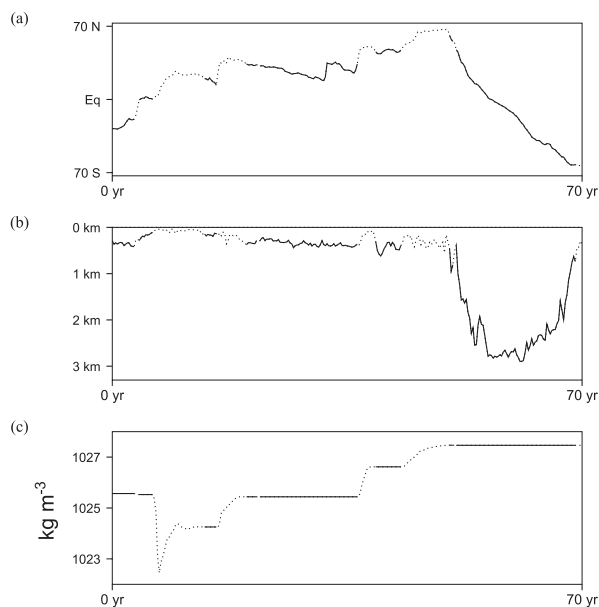


FIG. 3. Evolution of (a) latitude, (b) depth, and (c) density for an arbitrary water parcel during the last 70 yr of the nondiffusive simulation. Time segments in which the parcel has no contact with the surface are denoted with solid lines. Inspection of raw model data reveals that there is absolutely no change in density during each of these segments.

boundary current (years 50–70), during other periods without contact with the surface the parcel is never more than a few hundred meters deep (e.g., years 20–35).

It turns out that switching to a uniformly high vertical resolution does very little to change the stratification or circulation characteristics. In fact, it appears that after this entire 4000-yr period ocean adjustment toward a statistically steady state is nearly completed. This is confirmed by integral measures of the adjustment, including effects of the surface density forcing, the total kinetic energy, and the average density below 2 km, along with their derivatives (Fig. 4). Systematic variations in the integrated effects of surface density forcing decay rapidly after the simulation is started (Fig. 4a). Most of the kinetic energy adjustment occurs in the first few hundred years of the simulation, and then only relatively weak variations are present, presumably associated with meanders or other small variations in western boundary currents and the circumpolar current (Fig. 4b). Similarly, most of the adjustment in deep stratification (Fig. 4c) occurs in roughly the first 700 years of the nondiffusive simulation, with only a very weak increase in the density of the abyss at later times (less than 0.01 kg m^{-3} per 1000 yr after adjustment to the new resolution has occurred).

Note that a spinup period of several thousand years would be sufficient to expect a near steady state in a model run with a typical vertical diffusivity of $1 \text{ cm}^2 \text{ s}^{-1}$, which is

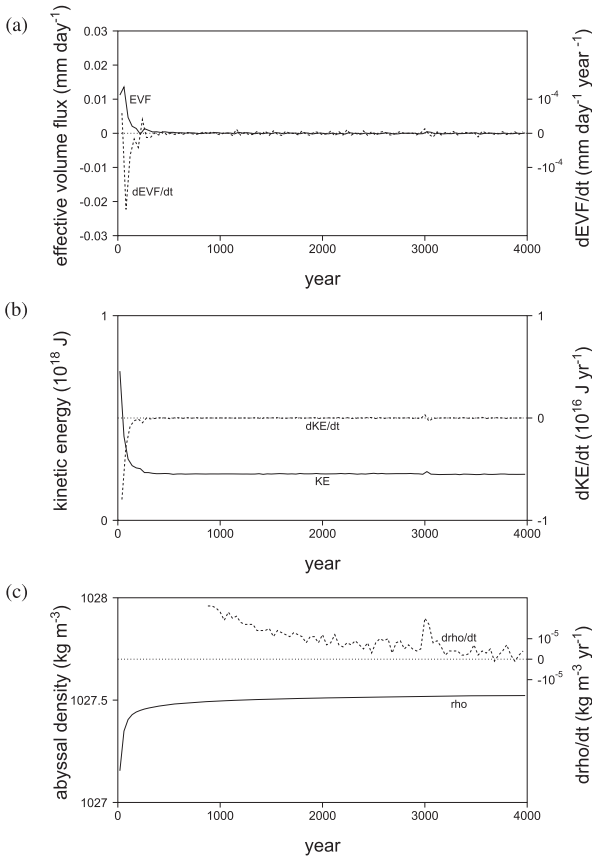


FIG. 4. Integral measures of adjustment toward a steady state: (a) average effective volume flux (EVF) resulting from density restoring at the ocean surface, (b) ocean total kinetic energy, and (c) average density below 2 km. In each panel, the average value of the stated variable over 40-yr time segments is plotted with a solid line, and its derivative with respect to time with a dashed line.

based on the appropriate diffusive time scale. However, there is no comparable time scale for the nondiffusive run. Rather, in this latter case the time scale of the adjustment relates to how fast the abyssal ocean fills with dense water that forms near the poles.

To illustrate the time scale of ocean ventilation we present a cumulative distribution of transit times for water parcels at the end of the nondiffusive simulation (Fig. 5a). The transit time for each parcel is defined as the time from the parcel's last contact with the surface to its current position, which is shown in Fig. 5a (solid line) for the end of the nondiffusive simulation (4000 yr). We see that roughly 70%–80% of the parcels have had contact with the surface in the last 1000 yr (Fig. 5a). In contrast, much of the bottom water ($z > 3000$ m) in the Northern Hemisphere requires more than 3000 yr for ventilation (Fig. 5b). When tracer diffusion is included, ventilation of this bottom water occurs at a much more rapid pace (Fig. 5a, dotted line; Fig. 5c).

Note that the transit time of a water parcel is a natural and simply defined concept for a Lagrangian model: that is, the time that has elapsed since the parcel was last at the surface. For a nondiffusive ocean the transit time (as defined above) and the water ventilation age are synonymous. However, for a diffusive ocean the two will differ because the ventilation age of a submerged parcel is an integral quantity that depends on the parcel's transit time and the effects of mixing with surrounding parcels. Since most of this study deals with a nondiffusive ocean, here we do not distinguish the parcel's transit time and ventilation age.

2) THE DIFFUSIVE OCEAN AND OTHER SIMULATIONS

Besides the featured nondiffusive simulation, we carry out an additional simulation to examine how ocean circulation and stratification change when tracer diffusion is included. The diffusive simulation uses the same resolution as the spinup run but includes a tracer diffusivity value varying linearly from $1.2 \text{ cm}^2 \text{ s}^{-1}$ at a 4.9-km depth to $0.3 \text{ cm}^2 \text{ s}^{-1}$ at the surface. Comparing density and flow fields for this simulation to those for the nondiffusive ocean illustrates the contributions of tracer diffusion to stratification and meridional overturning and how key water pathways are altered by the presence of diffusion. In addition, we carry out several experiments to test the sensitivity of overturning, stratification, and bolus transports to changes in the horizontal and vertical resolution of the model (see the appendix and section 3e) and to examine the impacts of the localized perturbation to the restoring density in the southern high latitudes on ocean stratification (section 3g).

3. Stratification and circulation in a nondiffusive ocean

In this section we examine circulation and density structure in an ocean with no tracer diffusion. Water parcels exactly conserve their densities when they are not in contact with the surface layer.

a. Surface features and horizontal circulations

The near-surface density and flow patterns for the run with zero interior diffusion are shown in Fig. 6a. Prominent features include western boundary currents, Ekman divergence over the equator with a weak dense (cold) tongue, a meandering circumpolar current, and an eastern boundary current in the northern subpolar region. As expected, boundary currents deflect isopycnals in the direction of the flow and, overall, density and flow patterns are not that different from typical density-diffusing simulations for idealized basins of this kind. Note that,

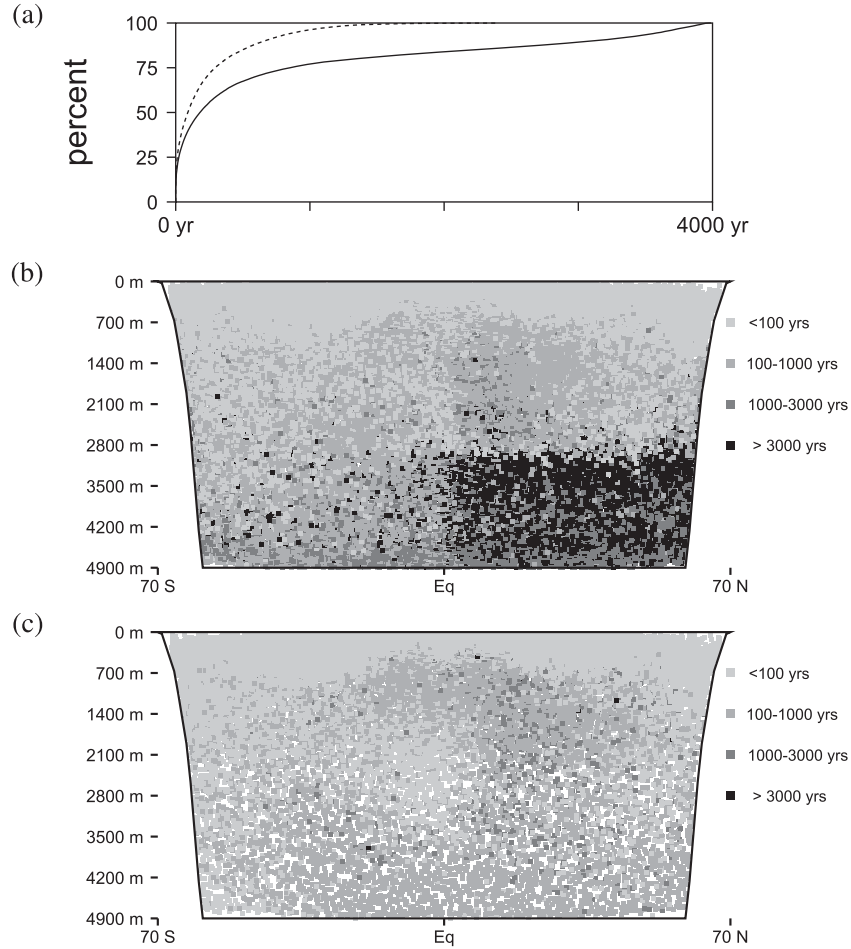


FIG. 5. (a) Cumulative distribution of transit times for all water parcels in nondiffusive and diffusive simulations (solid and dashed lines, respectively) at the end of each model run. The transit time is defined as the time it takes for a parcel to travel from the surface to its current position. Each parcel is marked with a shaded box to indicate its transit time for (b) nondiffusive and (c) diffusive simulations. This figure demonstrates that in the diffusive run a vast majority of the parcels have been in contact with the surface within the last 1000 yr. In contrast, in the nondiffusive run bottom water north of the equator is only very weakly ventilated, if at all, with many transit times exceeding 3000 yr.

although the eastern boundary current in the northern subpolar region causes a strong deflection in isopycnals, this is partly attributable to the weaker gradient in the restoring density north of 60°N (Fig. 2b); this current is actually much weaker than the western boundary current in the northern subtropics (Fig. 6a).

The horizontal streamfunction is shown in Fig. 6b. Circulations resembling classical Munk gyres appear in the Northern Hemisphere with a much weaker subtropical gyre and a strong circumpolar current in the southern portion of the basin. The Northern Hemispheric western boundary current transports roughly 35 Sv ($\text{Sv} \equiv 10^6 \text{ m}^3 \text{ s}^{-1}$), and the circumpolar current has an amplitude of about 120 Sv, both of which are broadly in

line with their counterparts in the Atlantic Ocean (e.g., Cunningham et al. 2007; Nowlin and Klinck 1986). The meanders of the circumpolar current suggest steering by bottom topography (e.g., Killworth and Hughes 2002).

The Southern Hemispheric subtropical gyre appears to be weaker than that in the north for two reasons: 1) the northward and southward flows in the deep overturning cell occur at different longitudes, and they enhance the western portion of the streamfunction for the Northern Hemispheric subtropical gyre but weaken the streamfunction for the western portion of the southern hemispheric subtropical gyre (Figs. 6b–d) and 2) the steady meander of the circumpolar current interferes with the flow of the subtropical gyre in the Southern

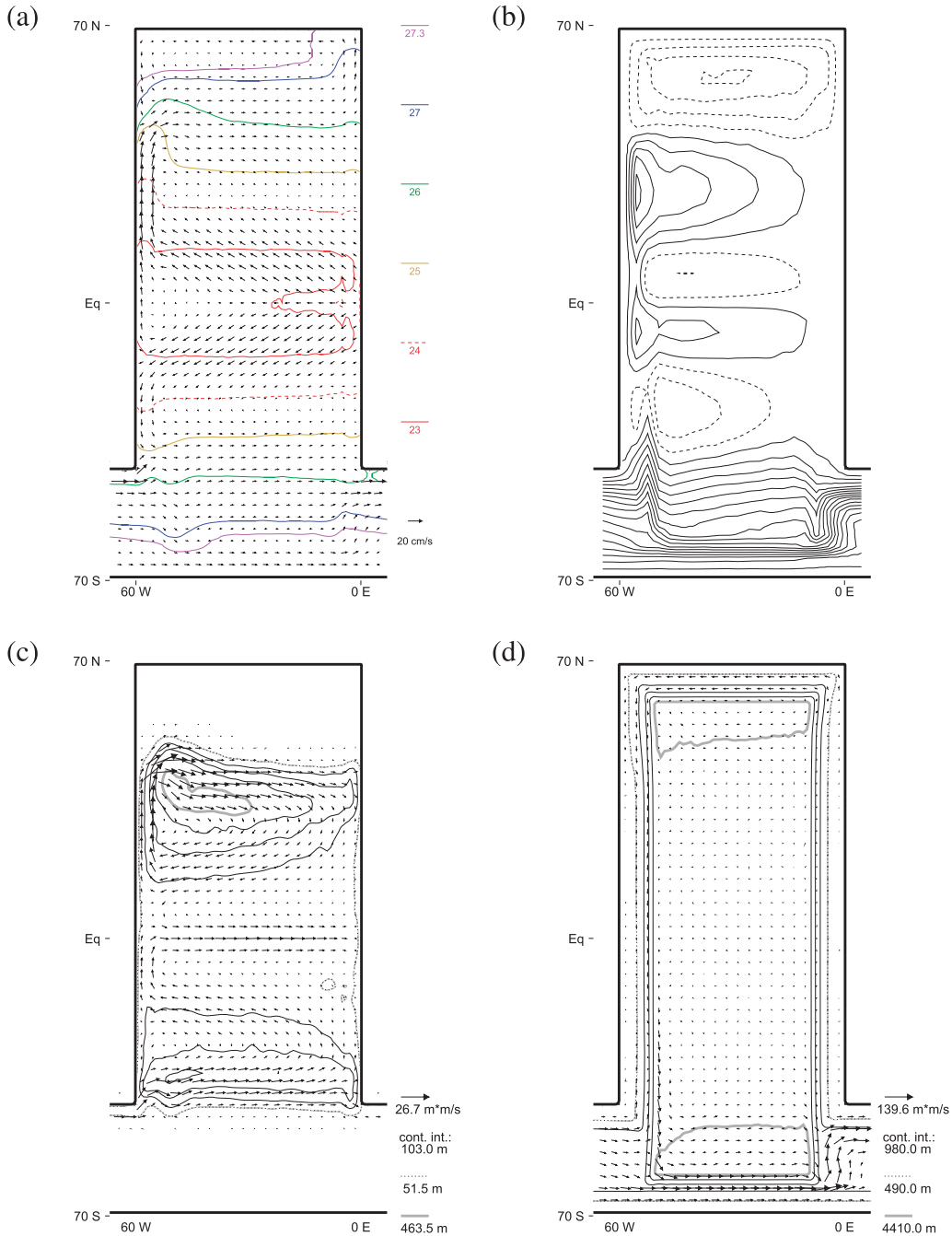


FIG. 6. Surface fields and horizontal flow for the nondiffusive ocean averaged for the last 30 years of calculations: (a) near-surface density (kg m^{-3}) and velocity, (b) barotropic streamfunction (contour interval 7 Sv), and layer thickness and transport for (c) the 1025–1026 kg m^{-3} density layer and (d) the 1027–1028 kg m^{-3} density layer. Note the equatorial cold tongue in (a) and the gyre systems and the ACC in (b). A branch of the ACC meanders northward and then back at about 60°W reminiscent of the Falkland (Malvinas) current.

Hemisphere. These points are illustrated by plots of transport and thickness for the 1025–1026 kg m^{-3} and 1027–1028 kg m^{-3} density layers (Figs. 6c,d). The former shows flow and thickness perturbations associated with

subtropical gyres (Fig. 6c), and the latter shows the positioning of the deep western boundary current (Fig. 6d), which maintains a nearly a constant transport from 50°N to 50°S.

b. Ocean density (thermal) structure

The subsurface ocean density structure in the non-diffusive ocean is not unlike that observed in the Atlantic Ocean (Fig. 7a), despite the idealized nature of the model. Each of the major water masses in the Atlantic is represented: warm surface tropical and subtropical waters stratified according to the ventilated thermocline theory (Luyten et al. 1983), Antarctic Intermediate Water (AAIW) that subducts between 40° and 60°S; North Atlantic Deep Water (NADW; or “deep water”) that forms north of 40°N; and Antarctic Bottom Water (AABW; or “bottom water”) that sinks south of 60°S (Fig. 7b). The main thermocline is about 800–900 m deep in most of the basin, and its overall shape is similar to that for the Atlantic, which is shown with the $\sigma_1 = 31.9$ contour line in Fig. 7a. In much of the ventilated thermocline, the main thermocline, and the deep ocean, simulated isopycnals run parallel to observed isopycnals. The tropical thermocline, which exhibits a much greater density gradient, reaches depths of about 250 m (Fig. 7a).

Because each water parcel’s density is only altered by surface forcing, it is essentially determined by the latitude ϕ_s at which the parcel last had contact with the surface. In Fig. 7b, we color code parcels according to their value of ϕ_s , which is found by following reverse trajectories for the last 700 years of the nondiffusive simulation. Simply by comparing Figs. 7a,b, one can explain most of the density structure in the idealized ocean. Water with a density of less than 1026 kg m^{-3} forms at latitudes between 40°S and 40°N and circulates within shallow tropical/subtropical cells. Most of the water with densities between 1026 and 1027 kg m^{-3} forms between 40° and 60°S, and it seems appropriate to refer to this water as Antarctic Intermediate Water. North Atlantic Deep Water forms north of 40°N and spans depths of 1–3 km in most of the ocean. Finally, Antarctic Bottom Water forms south of 60°S and spreads northward, slowly filling the ocean below about 3 km.

Note that Fig. 7b compares favorably with the observed salinity structure in the Atlantic (Fig. 7c), which suggests similar distributions and regions of formation for each of the major water masses in the Atlantic Ocean. In particular, the model generates a northward intrusion of AAIW that divides warm tropical and subtropical waters from deep water (Fig. 7b), similar to that in the observations (Fig. 7c).

Also note that in Fig. 7b we deliberately truncate trajectories at 700 years in order to illustrate the time scale of ventilation for bottom water. Although most of the bottom water in the Southern Hemisphere is ventilated on a time scale of less than 700 yr, most of the bottom water in the Northern Hemisphere is much older (Fig. 5b).

To examine the ocean thermocline structure more closely, we consider profiles of density for several locations and compare them to observations (Fig. 8). There are several clearly defined thermoclines in the non-diffusive ocean (e.g., Figs. 8a,b): the strong, upper-ocean ventilated thermocline centered at about 200-m depth; another (internal) thermocline located at the base of mode water and centered around 800 m; and a weaker internal thermocline separating NADW and AABW. The depth of this thermocline is about 2900 m in the middle of the basin and 2100 m near the basin southern boundary, which matches the depth of Drake Passage.

The structure of the upper two thermoclines is somewhat similar to that discussed by Samelson and Vallis (1997) and Vallis (2000). In their results the main thermocline also effectively splits into two parts: the upper-ocean ventilated thermocline that outcrops on isopycnals in the subtropical gyre and a deeper internal thermocline controlled by diffusion. In contrast, in our nondiffusive ocean this internal thermocline is a nondiffusive boundary layer between AAIW and NADW (Fig. 7b).

Overall, the comparison to observations (gray lines in Figs. 8a,c,e and gray boxes in Figs. 8b,d,f) reveals the same gross vertical structure of density for the nondiffusive ocean, except for a light density bias of $0.3\text{--}0.4 \text{ kg m}^{-3}$. The light bias results from a significant (negative) departure of the idealized restoring density from the observed surface density in low to midlatitudes (Fig. 2b) combined with the overly idealized representation of deep convecting regions.

c. Meridional overturning

A direct examination of the meridional overturning circulation (Fig. 9) reveals that the deep cell includes about 13 Sv of sinking water north of 30°N, and streamlines suggest that almost all of this water upwells in the Southern Ocean (Fig. 9a). There are also shallow, wind-driven tropical/subtropical cells and a Deacon cell (Doos and Webb 1994), a largely adiabatic overturning in the Southern Ocean with a local maxima in circulation at 51°S, 400 m.

Examining overturning with density as the vertical coordinate (Fig. 9b) yields a higher-resolution view of the shallow wind-driven cells, causes the Deacon cell to disappear as expected, and illustrates how water parcels that traverse the subsurface portion of the deep overturning cell (e.g., the deep western boundary current) maintain a constant density, with flat streamlines in the lower part of Fig. 9b. Overturning of bottom water is very weak [$O(1 \text{ Sv})$] and it barely registers in the lower-left region of Fig. 9b (note that, in our idealized ocean, bottom water has densities around or greater than 1027.5 kg m^{-3} , as shown in Figs. 7a,b).

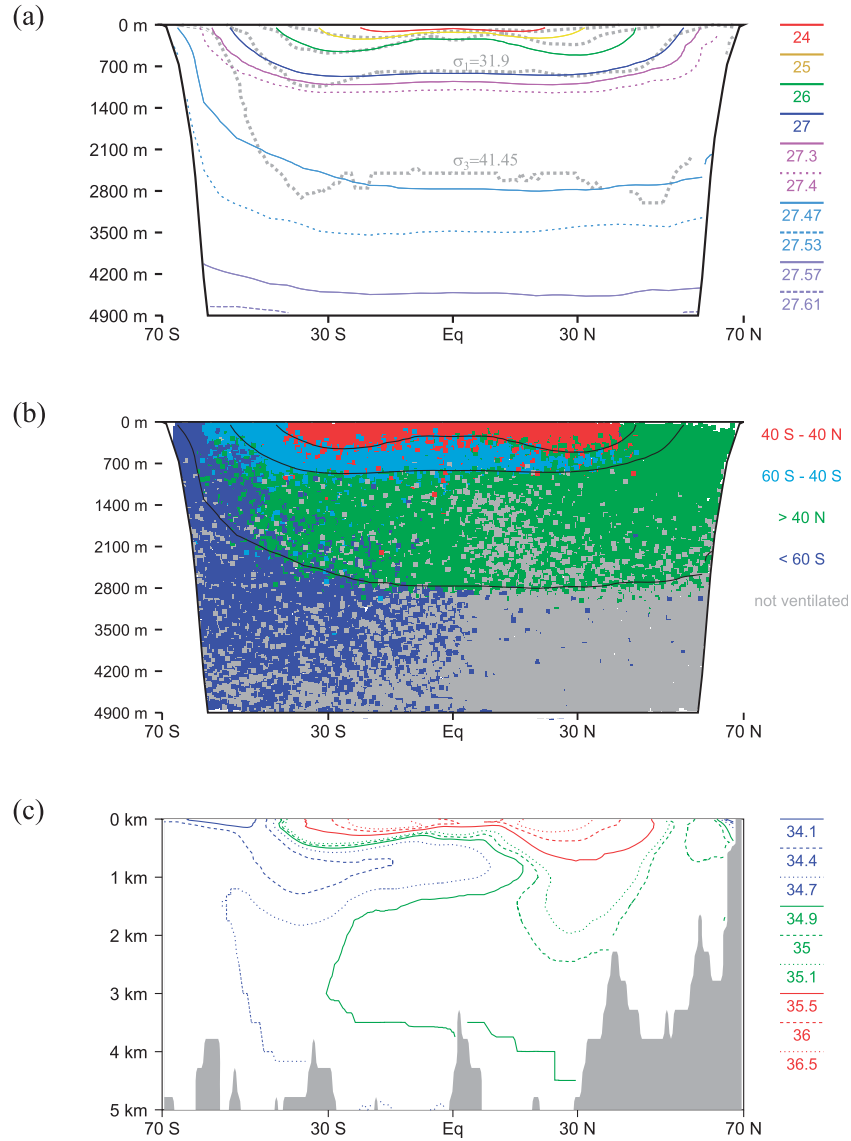


FIG. 7. Ocean density and water masses. (a) Simulated density along 30°W (colored contours), along with observed isopycnals (dashed gray lines) for $\sigma_0 = 26, 26.7$; $\sigma_1 = 31.9$; and $\sigma_3 = 41.45$ (where σ_n is potential density referenced to $n \times 1000$ dbar). Note the upper-ocean ventilated thermocline and an internal thermocline separating AAIW from NADW. (b) Water parcels shown as small squares colored according to the latitude at which they last had contact with the surface (showing different water masses). Black contours mark the 1026, 1027, and 1027.47 kg m^{-3} isopycnals. Parcels shaded gray were not ventilated during the last 700 years of the simulation; bottom water north of the equator primarily comprises such parcels. (c) Observed (Levitus) salinity (psu) along 30° W. Note that the LOM produces a northward intrusion of AAIW similar to that in nature.

d. Lagrangian analyses of water pathways

One advantage of our Lagrangian model is that it provides precise trajectories for every water parcel in the ocean with no added computations, allowing individual mass elements to be tracked over long periods of time. In

this section, we use this information to track circulation patterns for each of the major water masses identified in Fig. 7b. In particular, we address the following questions: where does sinking water ultimately upwell, and which water pathways make the largest contributions to the meridional overturning streamfunction?

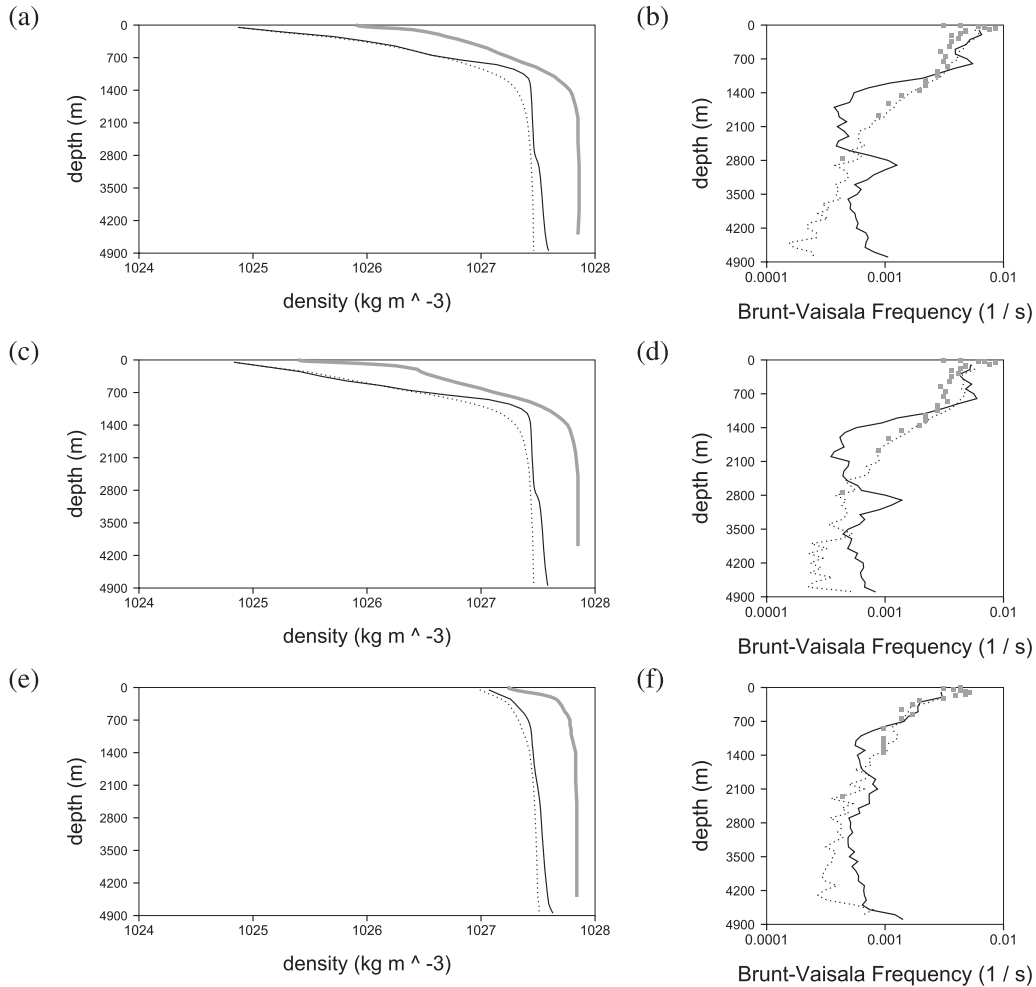


FIG. 8. Profiles of density and Brunt–Väisälä frequency as a function of depth for different locations for the nondiffusive (black lines) and diffusive (dotted lines) simulations at (a),(b) 30°N, 10°W; (c),(d) 30°N, 30°W; and (e),(f) 55°S, 30°W. Observed potential densities (gray lines) and Brunt–Väisälä frequencies (gray boxes) at the same latitudes in the middle of the Atlantic are also shown. Note the ventilated thermocline near the surface, the first internal thermocline centered at about 800-m depth [in (a)–(d)], and the second internal thermocline that separates NADW and AABW in the nondiffusive experiment. The depth of the second internal thermocline is about 2900 m in low latitudes and 2100 m in the southern high latitudes. The 0.3–0.4 kg m⁻³ offset between modeled and observed density profiles is a consequence of the idealized form of the restoring density (see text).

1) SUBDUCTION AND UPWELLING OF NORTHERN HEMISPHERIC WATER

In this section, we consider the fate of water parcels that subduct in the northern portion of the ocean basin. We examine trajectories during the last 70 years of the model run and select paths for all parcels that sink from the surface north of 30°N and upwell south of 10°N. It turns out that there are essentially two key pathways that satisfy these criteria, which we distinguish according to the latitude where the water subducts. Because plotting many trajectories at one time yields a

“spaghetti” diagram that is hard to interpret, we instead objectively identify pathways most frequented by water parcels that satisfy given upwelling and downwelling criteria. One important question to which this information provides a clear-cut answer is, where do parcels that sink in the Northern Hemisphere upwell?

Figures 10a,c illustrate the preferred pathway to upwelling for water that sinks north of 40°N in two coordinate systems. To construct a composite trajectory, we divide longitude/latitude and latitude/depth domains into 3° by 3° and 3° by 300 m bins, respectively, and contours indicate the percentage of trajectories that

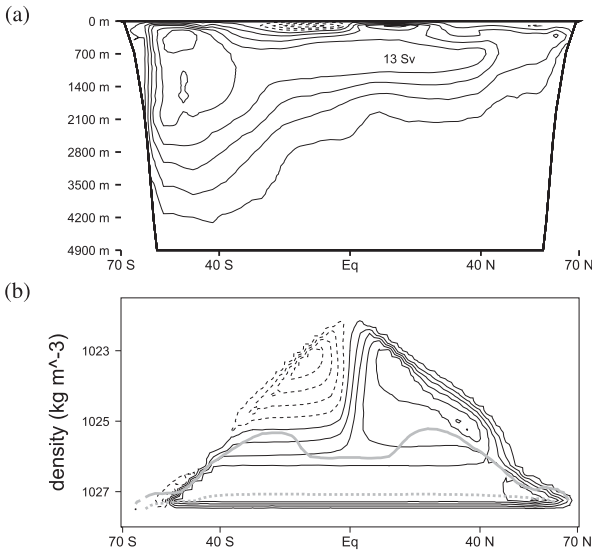


FIG. 9. Meridional overturning (contour interval 3 Sv) in (a) height and (b) density coordinates for the nondiffusive simulation. In (b) contours of average depth are for 300 (solid gray) and 1200 m (dotted gray). Note that streamlines are flat in the lower part of (b), indicating no density change in the lower branch of the deep overturning cell. The shallow subtropical cells are especially prominent in (b). The Deacon cell is prominent in (a) but absent from (b). The weak cell in the bottom-right corner of (b) indicates recirculation in the subpolar gyre. The cell in the bottom-left corner of (b) is apparently mostly a consequence surface density restoring along the boundary of the channel. Less than 1 Sv of the volume transport of this cell participates in ventilating the bottom ocean.

satisfy the given upwelling and downwelling criteria that pass through a given bin. For example, a contour value of 50% in Fig. 10a indicates that half of the parcels that sink north of 40°N and upwell south of 10°N during the last 70 yr of the simulation pass through a particular 3° by 3° region. This analysis reveals that parcels travel southward in the deep western boundary current (Fig. 10a), reaching depths from about 1 to 3 km between 40°S and 40°N (Fig. 10c) before upwelling in the Southern Ocean.

The preferred location of subduction is where the deep western boundary current starts in our model, that is, where dense water in the subpolar gyre plunges beneath relatively light water traveling northward in the near-surface western boundary current associated with the subtropical gyre (Fig. 6). Only a handful of parcels upwell at the equator, and all of these sink at latitudes between 40° and 45°N and remain less than 1 km deep. This result illustrates that without tracer diffusion deep water cannot contribute to the equatorial upwelling.

In contrast, all of the water parcels that sink from the surface between 30° and 40°N upwell near the equator (Figs. 10b,d), with a much shallower subsurface pathway and downwelling locations concentrated in the eastern

portion of the basin. The existence of distinct, well-defined subsurface pathways, like those illustrated in Figs. 7b and 10, is what leads to distinct regions of stratification in Fig. 7a, and examining such pathways helps one to understand how stratification develops in the nondiffusive ocean. Note that the pathway illustrated in Figs. 10b,d is generally consistent with ventilated thermocline theory (Luyten et al. 1983; Pedlosky 1996), as is the stratification shown in Fig. 7a.

Of course, the pathways in this model are much simpler than those of water parcels in nature owing to the idealized basin and low resolution (e.g., the lack of mesoscale eddies); yet, the model reproduces much of the density structure and the basic water mass distribution observed in the Atlantic Ocean, which validates our modeling approach (for a further discussion of this point, see section 4). Also note that our method of compositing illustrates the most rapid and direct paths to upwelling; slow and/or meandering paths to upwelling that take more than 70 yr to complete are not included in the composite trajectories shown in Fig. 10.

2) WATER THAT SUBDUCTS IN THE SOUTHERN HEMISPHERE

In the Southern Hemisphere, the pathway to upwelling for water that subducts in the shallow wind-driven cell of the ventilated thermocline is similar to its counterpart in the Northern Hemisphere, although in the southern cell some of the water also upwells near the western boundary (not shown). However, the fate of sinking water poleward of the tropical/subtropical cell is quite different (Fig. 11) and warrants a discussion.

Water that subducts between 40° and 60°S (i.e., Antarctic Intermediate Water) travels northward along the western boundary at depths around or less than 1 km (Figs. 11a,c). Some of it enters the equatorial undercurrent and upwells in the eastern portion of the basin, but most continues northward along the western boundary and upwells in a zonally broad region near 45°N.

Water that sinks poleward of 60°S circulates in the lower portion of the Deacon cell (Figs. 11b,d), with very little penetration north of the equator, with upwelling occurring in the Southern Ocean. Accordingly, the pathway depicted in Figs. 11b,d describes parcel trajectories within the adiabatic Deacon cell. Thus, this pathway is clearly distinct from the classical bottom cell, which has a much longer time scale and is very weak in the non-diffusive ocean.

3) PARTITIONING THE MERIDIONAL OVERTURNING CIRCULATION

Comparing the subsurface pathway to upwelling for North Atlantic Deep Water (Fig. 10c) with the meridional

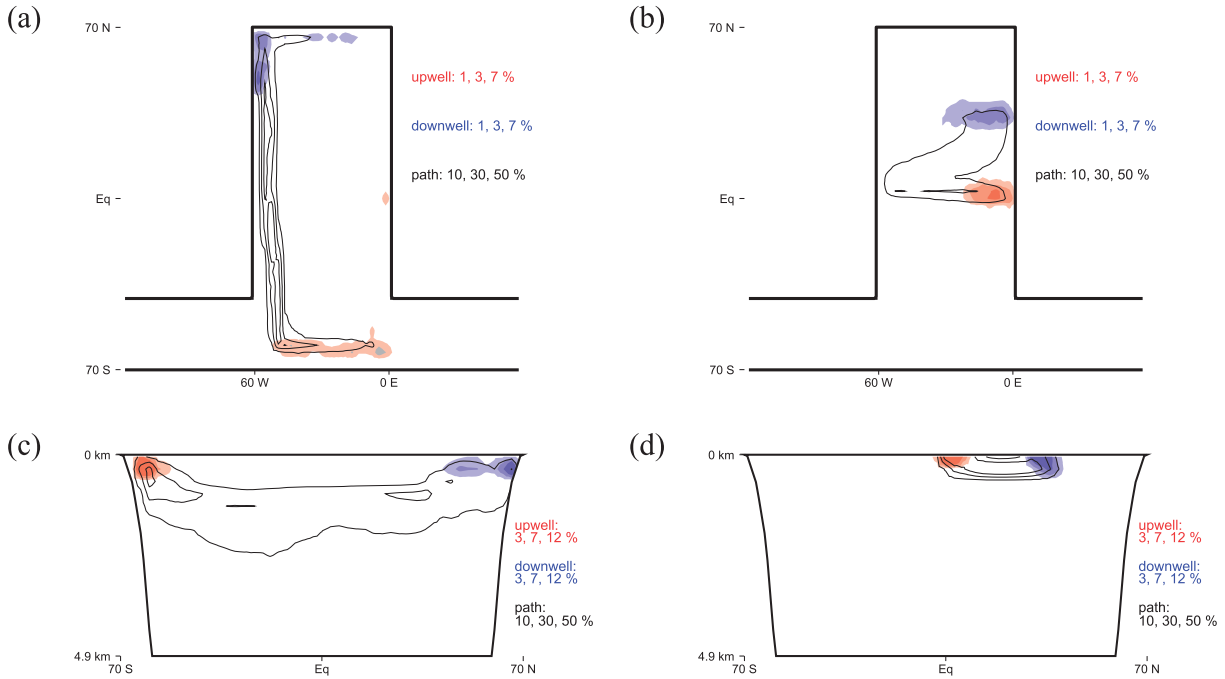


FIG. 10. Pathways to upwelling for water that subducts in the Northern Hemisphere in the nondiffusive ocean. (a),(c) Composite trajectory for all parcels that sink north of 40°N and upwell south of 10°N during the last 70 yr. (b),(d) Composite trajectory for all parcels that sink between 30° and 40°N and upwell south of 10°N during the last 70 yr. In each panel, black and white contours indicate the percentage of trajectories that pass within 3° and/or 300 m of a given location, and shading indicates the percentage of parcels that downwell (blue) or upwell (red) within 3° and/or 300 m of a given location. The duration of different trajectories ranges from 12 to 69 yr for (a),(c) and from 2 to 55 yr for (b),(d).

overturning streamfunction (Fig. 9a) brings up the following question: Why is the composite pathway to upwelling (Fig. 10c) much more shallow than the streamlines for the deep cell (Fig. 9a) in the southern portion of the basin? To address this question, and others like it, we seek a means of partitioning the meridional overturning circulation into components associated with particular water pathways. However, in general, arbitrary water pathways are not mass balanced and they do not have closed streamfunctions associated with them. To address this challenge we define a “complete path” as a parcel trajectory for which the starting and ending points have the same latitude. Note that, when a parcel traverses a complete path, there is zero vertically and temporally integrated meridional transport at every latitude. Two examples of complete paths are shown in Figs. 12a,c, one in which the parcel traverses much of the deep overturning cell (gray lines) and another in which a parcel remains confined to the Southern Hemisphere (solid lines).

Next, we consider all the parcel trajectories for the last 700 years of the nondiffusive simulation and break each into a series of complete paths and leftover incomplete paths. For a given parcel, each complete path starts and ends at the parcel’s initial latitude at the beginning

of the 700-yr period. In general, most parcels return to their starting latitude multiple times, yielding multiple complete path segments, but they typically do not end up at the same latitude at which they started. Therefore, the last leg of their journey is usually an incomplete path. We hypothesize that, to the extent that the incomplete paths represent a random sample of ocean circulations, excluding them will not change the structure of the overturning but reduce its amplitude. Indeed, we find that, by multiplying the streamfunction for all complete paths by 1.55 (not shown), we are able to obtain the gross structure of the streamfunction for all paths (Fig. 9a). Moreover, the complete path streamfunction can be partitioned in an arbitrary manner, yielding closed streamfunctions for each component of the partition. For example, Fig. 12b shows the streamfunction associated with all complete paths that remain south of 20°N, and Fig. 12d shows the streamfunction for all complete paths that pass north of 20°N at some point.

It is clear from these figures that the plunging of the streamlines toward the bottom in Fig. 9a is not associated with the classic, bottom overturning cell. Rather, it is parcels that meander northward and southward at different depths as they traverse the circumpolar current (e.g.,

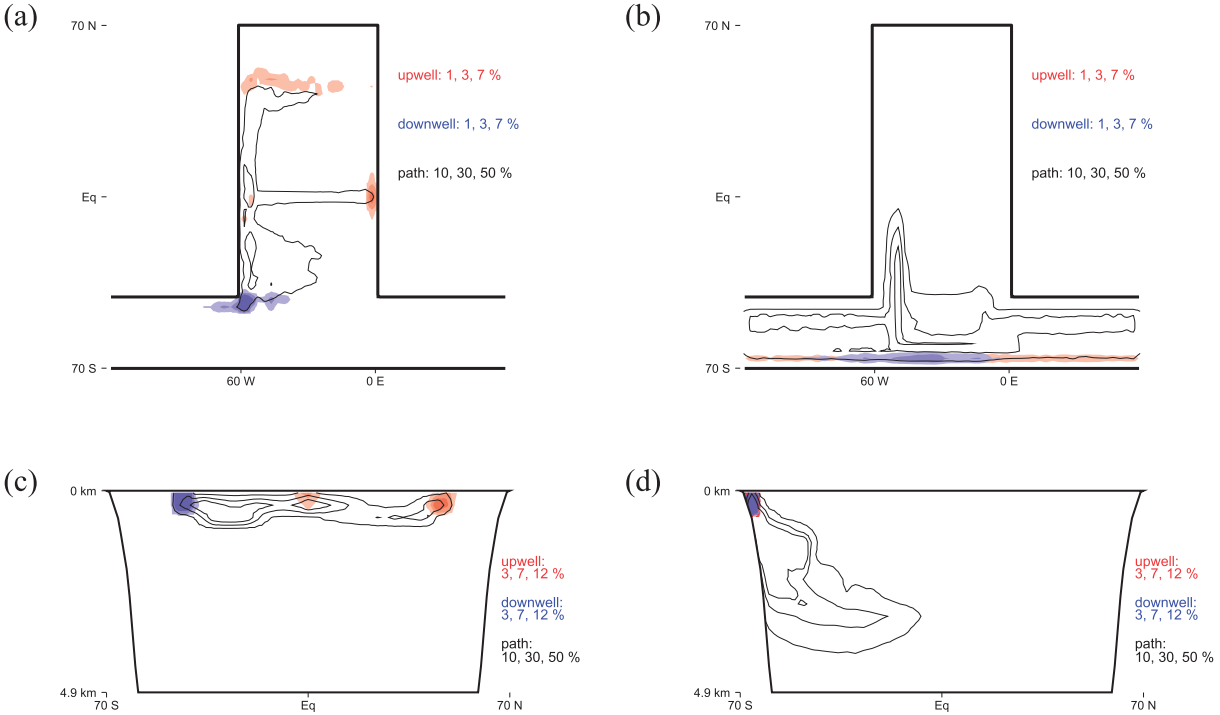


FIG. 11. Pathways for water that subducts in the Southern Hemisphere in the nondiffusive ocean. (a),(c) Composite trajectory for all parcels sinking between 40° and 60° S and upwelling north of 10° S in the last 70 yr of the nondiffusive simulation. (b),(d) Composite trajectory for all parcels sinking south of 60° S and advancing north of 30° S and to depths greater than 3 km prior to upwelling in the last 700 yr of the nondiffusive simulation. Contouring and shading as in Fig. 9. The duration of different trajectories ranges from 6 to 66 yr for (a),(c) and from 6 to 166 yr for (b),(d).

Figs. 12a,c, solid lines) that cause the very deep overturning in the Southern Hemisphere shown in Fig. 9a. Thus, the circulation depicted in Fig. 12b is essentially the Deacon cell for our idealized basin (Doos and Webb 1994). It results from the corkscrewing motion of a portion of the circumpolar current that occurs in response to variable bottom topography. We have found that this cell becomes shallower (i.e., more like the Deacon cell in nature) in preliminary experiments that use realistic topography instead of the idealized basin.

Our Lagrangian analysis and conclusions are largely consistent with those of Doos et al. (2008). However, in that study there were more water pathways contributing to the Deacon cell owing to the use of realistic topography and a global domain, and trajectories were truncated at 30° S, which may have reduced the contributions attributed to the circumpolar current.

When pathways that are confined to the south are removed from the total streamfunction, the residual streamfunction (Fig. 12d) becomes consistent with the pathway to upwelling for the deep cell (Fig. 10b). This residual streamfunction is analogous to the residual-mean circulation obtained in a zonally averaged model of the

Atlantic meridional overturning circulation (AMOC) by Sevellec and Fedorov (2011).

e. Bolus transports

One reason that our idealized ocean contains realistic density and overturning structures is that, even when run at a low resolution, the LOM spontaneously generates eddylike bolus transports. When a conventional ocean model is run at a coarse resolution, the GM parameterization is typically used to represent the transport of isopycnal layer thicknesses by unresolved eddies (e.g., Bryan et al. 1999). However, we have found no need to include such a parameterization in the LOM as the model spontaneously generates such a transport with approximately the right magnitude.

For example, Fig. 13 shows the meridional transport of the $1026\text{--}1027 \text{ kg m}^{-3}$ layer thickness by transient eddies (TE, solid lines) compared with what a GM parameterization would generate (GM, dashed lines) for a diffusion constant of $500 \text{ m}^2 \text{ s}^{-1}$ for 3° and 1.5° resolutions (Figs. 13a,b). The TE and GM transports are highly correlated, and the TE transport is similar at the two different resolutions. For the higher-resolution run, the TE transport

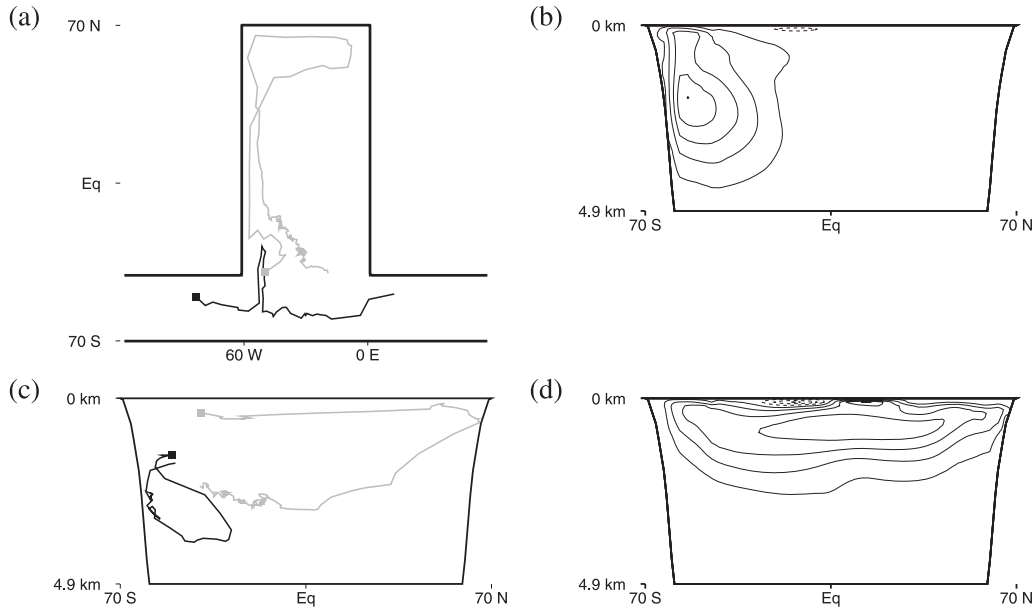


FIG. 12. Partitioning of the meridional overturning circulation into cross-hemispheric and Southern Hemispheric components: (a),(c) two examples of complete paths. The starting point of each path is marked with a shaded square. Note that the black path remains south of 20°N, the gray path passes north of 20°N, and each path finishes at the same latitude at which it starts. (b) Overturning streamfunction associated with all complete paths that remain south of 20°N during the last 700 yr of the nondiffusive simulation, which shows the model's equivalent of the Deacon cell (3-Sv contour interval). (d) Overturning streamfunction associated with all complete paths that pass north of 20°N at some point during the last 700 years of the nondiffusive simulation (contour interval 3Sv), which shows the deep cell isolated from the Deacon cell. In effect, this shows the model residual-mean circulation. The streamfunctions in (b),(d) are scaled to make up for the missing contribution of incomplete paths by multiplying by 1.55.

is slightly weaker in the vicinity of the Antarctic Circumpolar Current (ACC); however, in the higher-resolution run, the ACC exhibits stronger meanders (cf. Figs. 13c,d), suggesting a greater transport by standing eddies and opening up the possibility of eddy transports across the polar front in the zonal direction (evident at even higher-resolution runs but not shown here).

Rigorously explaining how the LOM generates these transports goes beyond the scope of this paper, but we do mention two key factors: 1) unlike in conventional models in which grid points are aligned in columns, in the LOM parcel centers are randomly distributed, leading to a better coverage of the horizontal domain, and 2) individual parcels can take paths that depart from the mean flow and are more like water pathways in nature and/or higher resolution runs. For an example of the latter, compare the parcel trajectory shown by the solid line in Fig. 12a with the mean flow of the ACC as indicated by Figs. 6b, 13c. The parcel makes a sharp and extensive northward loop (Fig. 12a), much more pronounced than that in the mean flow of the ACC (Figs. 6b, 13b) and more like the mean flow of the higher resolution run (Fig. 13d). Finally, there are hints that the generation of bolus transports in the LOM may have similarities to the horizontal mixing by

chaotic Lagrangian transport described by Rogerson et al. (1999) and Yuan et al. (2004).

f. Effects of including tracer diffusion

Although the focus of this paper is on the circulation and density structure that develop in an ocean with zero diffusivity, it is also instructive to include a realistic value for diffusivity to see how circulations and stratification change: that is, to pin down exactly what tracer diffusion contributes to the problem. In this section, we present a simulation that includes a vertical tracer diffusivity that varies linearly from 0.3 cm² s⁻¹ at the surface to 1.2 cm² s⁻¹ at 4.9-km depth (similar to the values used by Toggweiler and Samuels 1998). The model is run for 3000 years with this diffusion, which is more than enough time for the ocean to reach an equilibrium.

Figure 14 shows the density structure and the latitude at which parcels last had contact with the surface for the idealized ocean with tracer diffusion. Comparing this figure to Fig. 7 reveals several important changes caused by the presence of tracer diffusion. First, while the density of the upper ocean does not change much (Figs. 14a, 7a, 8), the main thermocline becomes less sharp. Second, diffusion decreases both the density and stratification of the

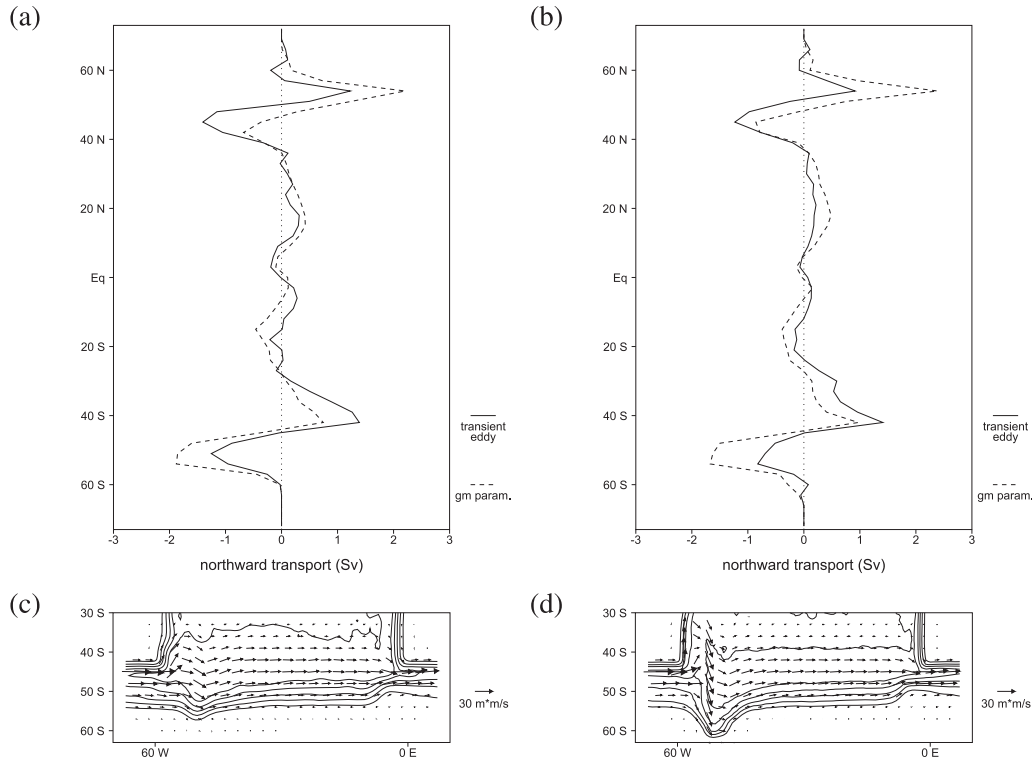


FIG. 13. Northward bolus transport of $1026\text{--}1027 \text{ kg m}^{-3}$ layer thickness for (a) 3° and (b) 1.5° model resolutions in nondiffusive runs (solid lines). The bolus transport is calculated by first calculating a time-average layer thickness H and meridional velocity v for each horizontal location and then computing $\int \overline{v'H'} dx$, where the prime notation denotes perturbations, the overbar a temporal average, x is the zonal distance, and the limits of integration are 62°W and 2°E . In each panel, the transport that a conventional GM parameterization would generate in this experiment is shown with a dotted line. A GM coefficient of $500 \text{ m}^2 \text{ s}^{-1}$ was used. Time-averaged $1026\text{--}1027 \text{ kg m}^{-3}$ layer thickness (100-m contour interval) and transport (vectors) for (c) 3° and (d) 1.5° resolutions. At the higher resolution, the transient eddy transport is reduced slightly in the Southern Ocean; however, steady meanders in the circumpolar current (i.e., standing eddies) become more intense. This figure demonstrates that, even with a relatively coarse resolution, the LOM can reproduce a realistic bolus transport without explicit eddy parameterizations such as GM.

abyssal ocean, which allows North Atlantic Deep Water to reach greater depths (as it does in nature). Third, although Fig. 14b suggests that each of the major water masses are transported downward and horizontally in a similar manner to that indicated by Fig. 7b, when tracer diffusion is present the boundaries between water masses become less distinct. For example, in Fig. 7a, AAIW remains largely isolated from water masses above and below it well to the north of the equator, but in Fig. 14b there is a substantial intrusion of North Atlantic Deep Water into the AAIW in the tropics.

We more precisely quantify density and stratification changes caused by vertical tracer diffusion by examining vertical profiles of density and Brunt–Väisälä frequency for several locations for both diffusive and nondiffusive runs (Fig. 8). We see that including diffusion does not alter the density of the upper ocean much (Figs. 8a,c,e); rather, it simply “rounds off” the inflection point in density near

the bottom of the main thermocline. In other words, diffusion makes the internal thermocline at the base of the mode water less sharp. However, this change significantly affects the vertical gradient in density and the Brunt–Väisälä frequency, making it more realistic (Figs. 8b,d,f). Moreover, the second internal thermocline formed at the boundary between North Atlantic Deep Water and Antarctic Bottom Water (Figs. 8b,d) in the nondiffusive ocean disappears when diffusion is included.

Although including diffusion increases the amplitude of the deep ocean overturning cell by several sverdrups (cf. Figs. 15a, 9a), the bulk of the transport and the overall structure of the cell is reproduced in the adiabatic limit. Diffusion also generates a realistic bottom overturning cell (Fig. 15a), leading to much more rapid ventilation of bottom water in the Northern Hemisphere (Figs. 14b, 5), which is more consistent with observations (e.g., Orsi et al. 2001).

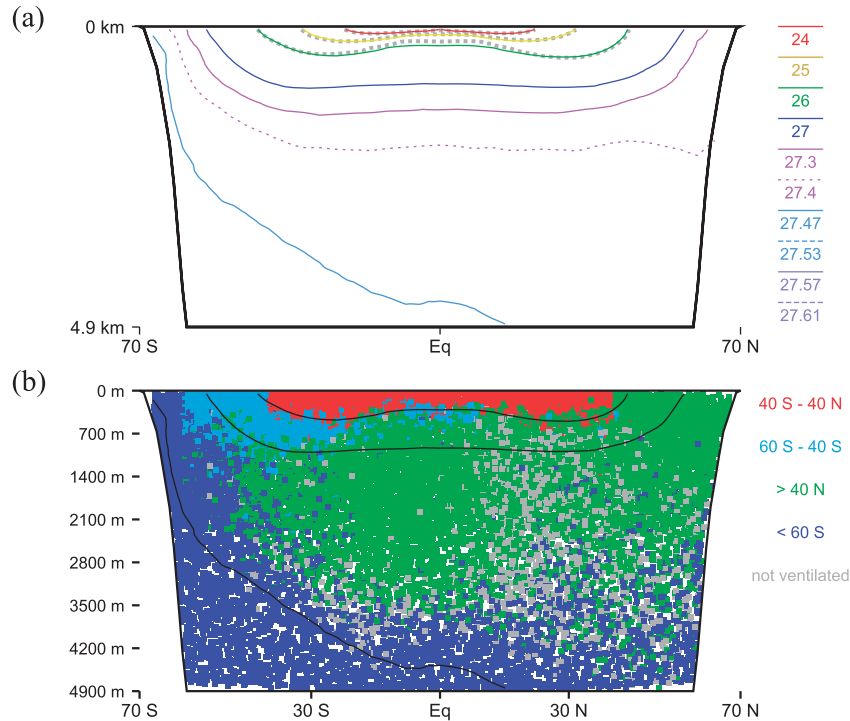


FIG. 14. Ocean density structure and different water masses for the simulation with tracer diffusivity ranging from $0.3 \text{ cm}^2 \text{ s}^{-1}$ at the surface to $1.2 \text{ cm}^2 \text{ s}^{-1}$ at 4.9 km: (a) density along 30°W (colored contours) along with the 1024, 1025, and 1026 kg m^{-3} isopycnals for the nondiffusive simulation (gray dashed lines). (b) Water parcels shown as small squares colored according to the latitude at which they last had contact with the surface during the last 700 yr of the diffusive simulation, which illustrates different water masses. Parcels shaded gray were not ventilated during this time frame. Black contours mark the 1026, 1027, and $1027.47 \text{ kg m}^{-3}$ isopycnals.

Finally, by converting density into temperature we estimate the oceanic northward heat transport for both the nondiffusive (solid) and diffusive (dashed) simulations (Fig. 16). Here, we have assumed that density variations are proportional to temperature variations times a thermal expansion coefficient of $0.2 \text{ kg m}^{-3} \text{ K}^{-1}$. This figure suggests that the bulk of the heat transport is carried out by adiabatic, wind-driven ocean circulation. In most of the domain, the simulated heat transport in our nondiffusive ocean is in the range of estimates for the Atlantic Ocean based on observations (Fig. 16b; adapted from Ganachaud and Wunsch 1993).

The estimated northward heat transport in the run with diffusion is generally 10%–20% higher than that for the nondiffusive ocean. This difference would have been even smaller if the Pacific basin were included in consideration.

g. Effects of localized deep convection

As we note in section 2, we include a localized perturbation to the restoring density near the southern boundary to cause deep convection to be localized, as it is in nature. In this section, we present the results of a 3000-yr

simulation identical to the spinup run except that it employs a zonally symmetric restoring density (Fig. 2b) without the perturbation near the southern boundary. The primary change associated with using this alternative restoring density is a decrease in the density and stratification of bottom water (Fig. 17a), which leads to a deeper and stronger deep cell (Fig. 17b) and NADW penetrating closer to the bottom (cf. Figs. 17c, 7b).

This run illustrates several key points. In general, it is not necessary to include localized perturbations to the restoring density profile to reproduce the gross stratification, water mass distribution, and overturning structure observed in nature. On the other hand, small perturbations to the restoring density in the Antarctic can have large impacts on abyssal stratification, so including tracer diffusion is not the only way to obtain more realistic deep/abyssal stratification.

4. Summary and discussion

In this study, we examine the circulation and density structure in an idealized ocean with a diffusivity of zero.

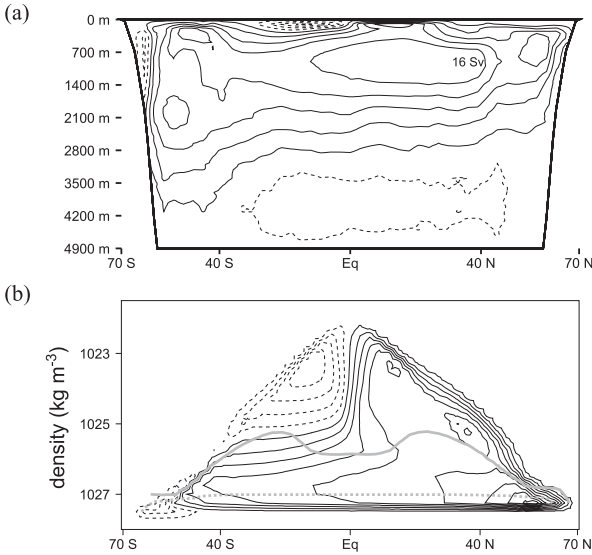


FIG. 15. Meridional overturning (contour interval 3 Sv) for the diffusive ocean in (a) height and (b) density coordinates. In (b) contours of average depth are for 300 (solid gray) and 1200 m (dotted gray). Note the well-developed bottom overturning cell as well as upwelling of deep water induced by vertical mixing.

The ocean basin is roughly the size of the Atlantic and it includes an extended periodic circumpolar channel. We apply a zonal wind stress and a surface density restoring function that are analytic approximations of those observed over the Atlantic. We also conduct a simulation with identical surface forcing that includes a moderate amount of interior diapycnal diffusion, as well as several other simulations that test sensitivities to model resolution and the structure of the restoring density.

With zero diffusivity, the idealized ocean develops a stratification not unlike that seen in nature, which amounts to a layering of water masses formed at different latitudes. Each of the major water masses in the Atlantic is represented: light subtropical and tropical waters in a ventilated thermocline, Antarctic Intermediate Water that forms between 40° and 60°S and spreads northward under subtropical waters, North Atlantic Deep Water that forms north of 40°N and occupies most of the ocean at depths between 1 and 3 km, and Antarctic Bottom Water that sinks south of 60°S and fills depths greater than 3 km.

The idealized ocean also develops a strong deep meridional overturning that comprises two components: a Deacon cell or adiabatic overturning associated with meandering and/or corkscrewing of a portion of the circumpolar current (Doos and Webb 1994; Doos et al. 2008) and the classic deep cell in which water sinks in the North Atlantic, travels southward in a deep western boundary current, upwells in the Southern Ocean, and is converted

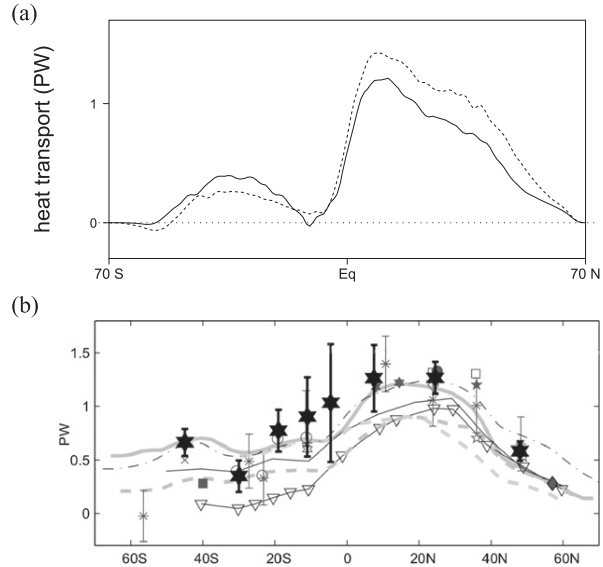


FIG. 16. A comparison of simulated and observed heat transport: (a) oceanic northward heat transport for the nondiffusive and diffusive simulations (solid and dashed lines, respectively) and (b) a variety of estimates of northward heat transport for the Atlantic Ocean adapted from Ganachaud and Wunsch (1993) (refer see Fig. 3 of that study for details on these estimates).

to AAIW before returning northward beneath the tropical/subtropical cells.

The deep overturning cell associated with the NADW in our nondiffusive ocean (13 Sv) is somewhat weaker than recent observations indicate (e.g., 18.7 ± 5.6 Sv in Cunningham et al. 2007). However, there are a number of factors unrelated to diffusion that can account for the difference. These include the relatively low vertical resolution of the model (a higher resolution increases the overturning as shown in the appendix) and the specified depth of the circumpolar channel (a deeper channel results in stronger overturning, as will be discussed elsewhere). Thus, our simulations suggest that it is quite possible that a nondiffusive ocean could support a deep overturning within the error bars of that observed in the Atlantic Ocean.

One intriguing aspect of the nondiffusive simulation is that, despite the fact that major ocean currents are underresolved and that water parcels are much larger than mesoscale eddies, the gross density structure and water mass distribution of the Atlantic Ocean is reproduced. One reason for this result is that, even at very low resolution, the Lagrangian model spontaneously generates bolus transports of isopycnal layer thickness having an amplitude and structure similar to that which a GM eddy parameterization would produce. Moreover, due to its Lagrangian nature, the model perfectly conserves every

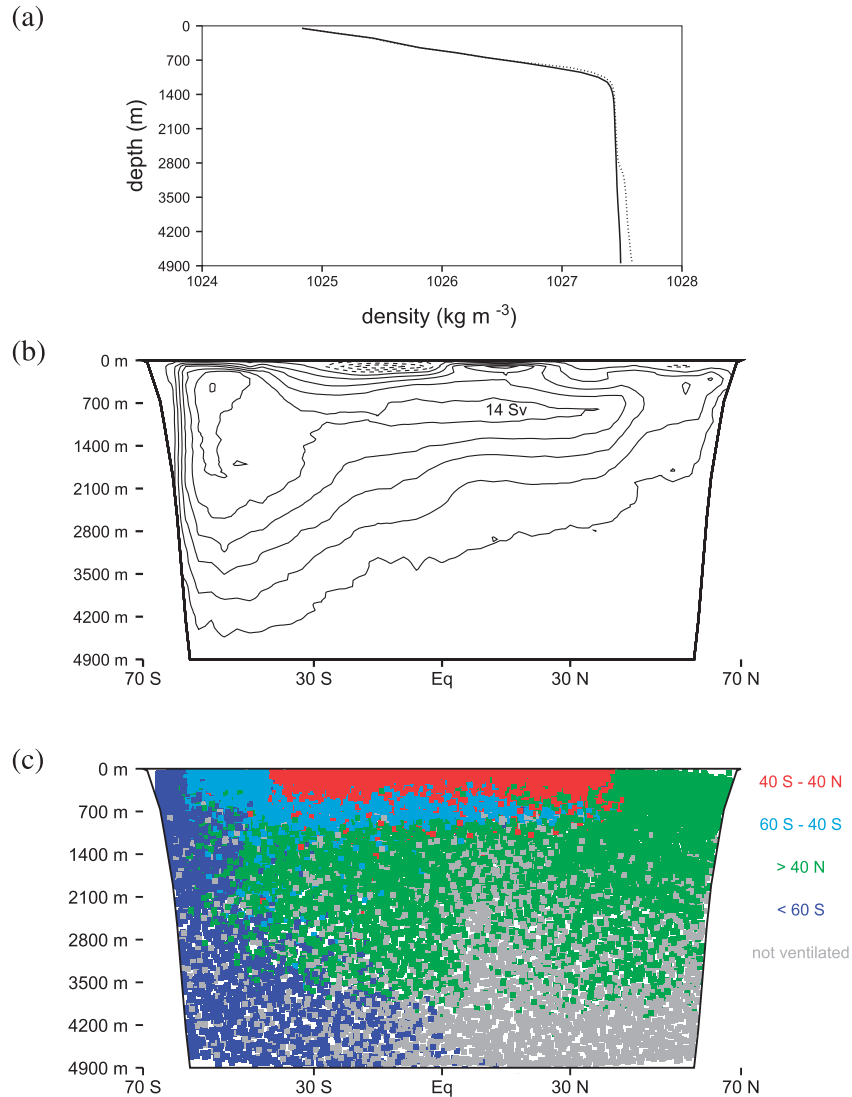


FIG. 17. Results for the nondiffusive simulation with a zonally symmetric restoring density: that is, lacking the perturbation near the southern boundary. (a) Density profile at 30°N, 30°W (solid line). (b) Meridional overturning (contour interval 3 Sv). (c) Different water masses. Colors indicate the location of each parcel's last contact with the surface during the last 700 yr of the simulation. The density profile for the original experiment (with a localized perturbation to the restoring density) is shown with a dashed line in (c).

moment of tracer distributions, so its low resolution does equate with excessive spurious diffusion, as can be the case for Eulerian models (Griffies et al. 2000).

We also note that major large-scale components of ocean circulation appear to be adequately resolved, including Ekman transport in the surface layer, equatorward Sverdrup flow in the interior of the ventilated thermocline, and regions of light and dense water formation at the surface. Is it possible, to the extent that boundary currents compensate for imbalances generated by these large-scale features and that the gross

effects of mesoscale eddies are accounted for by bolus transports, that the fine structure of currents and mesoscale circulations is not of zero-order importance for the density structure and water mass distribution in the oceans? Increasing the resolution of our nondiffusive ocean to the mesoscale, which we hope to do in the future, might help to address this important question.

A fundamental result of this study is that the nondiffusive model generates a realistic northward heat transport in the Atlantic (~1.2 PW). This result is consistent with the conclusion of Boccaletti et al. (2005), who introduced “heat

function” to argue that most of the ocean heat transport is done by the shallow surface-intensified circulation.

The modeling results and Lagrangian analysis presented in this study provide a complimentary perspective on the overturning circulation in the Southern Ocean to that of the residual-mean theory of Marshall and Radko (2003) and its extension in Sevellec and Fedorov (2011). A Lagrangian transport pathway like that shown in Fig. 12d develops because eddy transports cancel out much of the Ekman transport in the Southern Ocean. Whereas the studies of Marshall and Radko (2003) and Sevellec and Fedorov (2011) invoked the effect of transient meso-scale eddies, our Lagrangian analysis emphasizes the three-dimensional nature of the flow and, in particular, the effect of stationary eddies. Although there are bolus transports in the LOM (Fig. 13) analogous to those typically attributed to mesoscale eddies, their contribution is smaller than that of the meander in the ACC, which is essentially a large standing eddy (Figs. 6, 13). A recent high-resolution modeling study by Ito et al. (2010) also suggests that transports by standing eddies may do more to cancel Ekman transport over the Southern Ocean than transient eddies.

The nondiffusive ocean develops several clearly defined thermoclines. We note the strong ventilated thermocline centered at about 200-m depth and an internal thermocline at 800 m (Figs. 7, 8). This structure is somewhat similar to that in the double-thermocline model of Samelson and Vallis (1997) and Vallis (2000) for low-diffusion regimes. Their internal thermocline, however, is controlled by diffusion, whereas in our case it represents a nondiffusive boundary layer between Antarctic Intermediate Water and North Atlantic Deep Water. Therefore, our internal thermocline is effectively ventilated as well, with a broad region of source regions for the water contained in it. It is noteworthy that at depths in the nondiffusive ocean a weaker, second, internal thermocline is formed at the boundary between NADW and Antarctic Bottom Water. Vertical stratification between the two internal thermoclines remains very weak.

There are several notable features of the nondiffusive ocean that are inconsistent with observations. For example, the deep ocean below the main thermocline and above roughly 3 km develops almost no stratification and becomes separated from bottom waters by a weak but well-developed pycnocline. Available observations do not support the existence of this second permanent pycnocline even though it may still be possible in some regions of the ocean.

The bottom overturning cell in our nondiffusive simulation is also very weak, on the order of 1 Sv, and it appears to be weakening with time. Whether the bottom overturning cell will eventually disappear in the nondiffusive experiment (on time scales longer than used in this study) is unclear at this point. It is feasible that there

will remain a very weak bottom overturning cell related to inherent model turbulence allowing individual parcels from the ocean abyss to reach the surface on rare occasions. This question, however, is not critical since with higher diapycnal diffusion the strength of the bottom cell increases to almost 7 Sv, which better agrees with observations for the Atlantic (e.g., Talley et al. 2003).

The weakness of the bottom cell in the adiabatic simulation explains another property of the nondiffusive ocean—by changing the restoring density near the basin’s southern boundary (Fig. 2c) we can produce an arbitrary vertical stratification in the abyss. In fact, using a weaker localized density perturbation near the southern boundary would reduce the simulated stratification in the abyssal ocean to more realistic values (Fig. 17a) and allow a deeper penetration of NADW into the ocean.

Despite the idealized bathymetry, the relatively coarse model resolution, and the lack of atmospheric coupling, the nondiffusive ocean reproduces the gross stratification, water mass distribution, and meridional overturning observed in the Atlantic Ocean. Therefore, we conclude that surface forcing and adiabatic interior circulations fundamentally determine the leading-order density and circulation structure for the ocean, whereas tracer diffusion causes some important first-order perturbations including a higher, more realistic, stratification just below the main thermocline, an increase in the amplitude of deep overturning of several sverdrups, an increase in northward heat transport in the Atlantic of 10%–20%, and a realistic bottom overturning cell.

Acknowledgments. This research was supported in part by grants from NSF (OCE-0901921), Department of Energy Office of Science (DE-FG02-08ER64590), and the David and Lucile Packard Foundation. We thank George Philander, David Marshall, Bill Young, Rui Xin Huang, Geoff Vallis, Joe Pedlosky and Taka Ito for several discussions of this topic.

APPENDIX

The Lagrangian Ocean Model

a. Parcel shapes

The Lagrangian ocean model (LOM) represents a body of water as a collection of conforming water parcels. An understanding of how the LOM works starts with knowing the details of how water parcels are constructed. The vertical thickness H of each parcel satisfies the following equation:

$$H(x', y') = H_{\max} p\left(\frac{|x'|}{r_x}\right) p\left(\frac{|y'|}{r_y}\right), \quad (\text{A1})$$

where H_{\max} is the parcel maximum vertical thickness, r_x and r_y are the parcel radii in the x and y directions, the prime notation denotes a coordinate system centered on the parcel, and p is a third-order polynomial: $p(x) = 1 + (2x - 3)x^2$ for $x < 1$ and $p(x) = 0$ for $x \geq 1$. Figure A1a illustrates the bell-shaped vertical thickness distribution, and Fig. A1b shows how a collection of parcels that satisfy (A1) can have a variety of shapes. The vertical positions of parcels are determined by their “stacking order,” which is best visualized by thinking of placing the parcels in the basin one at a time with a parcel’s rank in the stacking order corresponding to its rank in the order of placement.

Despite the complexity of the shapes shown in Fig. A1b, it is relatively easy to define the parcel surfaces mathematically. The top of the n th parcel is given by the following formula:

$$b + \sum_{i=1}^n H_i(x - x_i, y - y_i), \quad (\text{A2})$$

where $b(x, y)$ is the height of the bottom topography and (x_i, y_i) denotes the horizontal position of the i th parcel. In other words, (A1) only constrains a parcel’s vertical thickness; its shape is also determined by the height of its lower surface, which depends on the height of the bottom topography and the thicknesses of the parcels below.

We use parcel radii r_x and r_y that are fixed in time, which means that a parcel’s vertical thickness function is not distorted by the flow. While this aspect of the LOM’s parcels is different from that of water parcels in the ocean, it means that there is no need to remap water mass to parcels after the initialization of the model, and individual parcels can be tracked for thousands of years. Moreover, because fluids are continuous (as we think of them) and numerical representations of them are discrete, every ocean model must have some sort of discretization along these lines that has no counterpart in a real ocean.

b. Parcel density and maximum vertical thickness

The version of the LOM used in this study predicts changes in a parcel’s density ρ using the following equation:

$$\frac{d\rho}{dt} = \Delta\rho_{\text{sf}} + \Delta\rho_{\text{diff}}, \quad (\text{A3})$$

where the subscripts “sf” and “diff” denote changes due to surface forcing and tracer diffusion, respectively. The surface forcing is a restoring to a prescribed surface density with a piston velocity (Griffies et al. 2009) of about 1 m day^{-1} . The implementation of tracer diffusion is discussed briefly below and in more detail by Haertel et al. (2004, 2009). Note that for the featured simulation presented

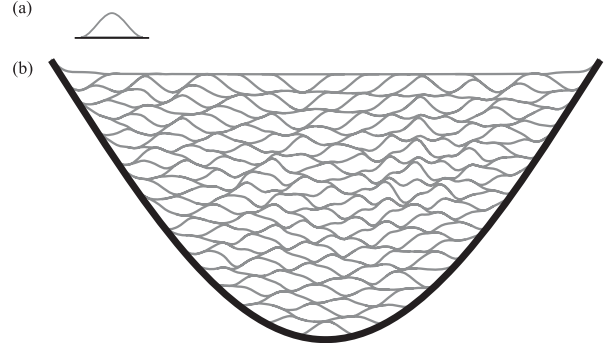


FIG. A1. Schema of how the LOM represents a body of water as a collection of conforming parcels: (a) the shape of a single water parcel when placed on a level surface and (b) a collection of water parcels in an idealized basin, each with the same thickness distribution from its center as that shown in (a). The ocean is in a hydrostatic equilibrium and no surface forcing is applied. The thickness of each parcel as a function of distance from its center is given by Eq. (A1). Adapted from Haertel and Straub (2010).

here the rightmost term in (A3) is set to zero so that a parcel’s density is exactly conserved when it is not in contact with the surface. The amount of mass associated with each parcel is fixed in time. Therefore, unlike models using the Boussinesq approximation, the LOM conserves the total mass, not the ocean volume. A parcel’s maximum vertical thickness is determined as follows:

$$H_{\max} = \frac{M}{\rho r_x r_y}, \quad (\text{A4})$$

where M is the parcel mass. In other words, the model predicts changes in density using (A3) and then diagnoses H_{\max} using (A4). The LOM can also be configured to predict changes in temperature and salinity independently and to calculate density using an equation of state, but we do not make use of these capabilities in this study.

c. Equations of motion

Horizontal motions of parcels are predicted using Newtonian mechanics:

$$\frac{d\mathbf{x}}{dt} = \mathbf{v} \quad (\text{A5})$$

and

$$\frac{d\mathbf{v}}{dt} + f \mathbf{k} \times \mathbf{v} = \mathbf{A}_p + \mathbf{A}_m, \quad (\text{A6})$$

where \mathbf{x} denotes horizontal position, \mathbf{v} is horizontal velocity, t is time, f is the Coriolis parameter, \mathbf{k} is the unit vector in the vertical, \mathbf{A}_p is the acceleration resulting from pressure, and \mathbf{A}_m is the acceleration resulting from

momentum exchange with nearby parcels (i.e., horizontal and vertical viscosity). To simplify the calculation of \mathbf{A}_p , which is an integral of the inward normal vector times pressure over the entire surface of a parcel, it is assumed that pressure is hydrostatic and that density is spatially uniform within a parcel, which yields the following formula:

$$\mathbf{A}_{p_i} = \frac{1}{M_i} \int g \nabla H_i \left[\sum_{j=i+1}^k (\rho_j - \rho_i) H_j + \rho_i \left(b + \sum_{j=i}^k H_j \right) \right] d\mu, \quad (\text{A7})$$

where the integral is evaluated over the horizontal projection of parcel i , g is gravity, k is the total number of parcels, and $d\mu$ is the horizontal area measure. We approximate (A7) with a Riemann sum, which leads to the conservation of energy in the limit as the time step approaches zero and requires $O(k)$ operations to evaluate for k parcels (Haertel and Randall 2002).

In this study we use a form of gravity wave retardation (Jensen 1996) that slows external gravity waves by a factor of 10. Physically speaking, this is done by assuming that, rather than displacing air, water parcels displace a fluid with a density of 1017 kg m^{-3} , which is roughly 99% of the average density of the ocean. This fluid is represented in (A7) as the k th parcel, and it is assumed to have a perfectly level free surface.

Equations (A5) and (A6) are solved at each time step to find new locations for the centers of the parcels. Note that in theory it would be possible for the parcels to disperse, creating a void. However, in practice this does not happen, because divergent flow creates a depression in the free surface, which causes a pressure gradient that accelerates parcels toward the center of the depression. In other words, the pressure force acting alone tends to produce circulations that level out the free surface, as is the case for bodies of water in nature.

d. Convective parameterization

The LOM employs a representation of convection that is unique to its Lagrangian framework. After each time step parcel stacking orders are sorted by density so that dense parcels lie beneath not so dense parcels. Figure A2 illustrates the effects of this convective adjustment scheme. In the event that surface forcing or diffusion causes a local unstable stratification (i.e., a dense parcel to lie above a not so dense parcel), the vertical positions of the offending parcels are swapped so that a stable stratification is restored. We have explored the potential ramifications of this unique convective parameterization in a Lagrangian model of the atmosphere and obtained very

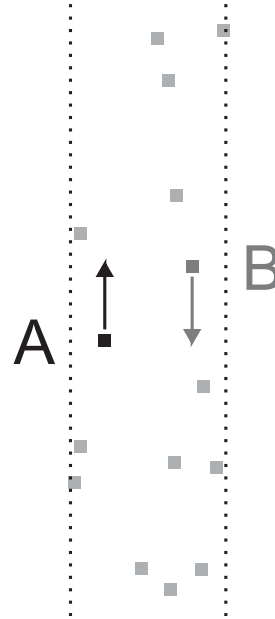


FIG. A2. The convective adjustment scheme: locations of a collection of parcels within a model column are marked with boxes. Parcel A is less dense than parcel B, and the convective scheme simply switches their vertical positions (i.e., stacking order) to restore a stable stratification. Adapted from Haertel and Straub (2010).

encouraging results, with atmospheric convective systems appearing to be more realistic than those generated by conventional atmospheric climate models (Haertel and Straub 2010).

e. Viscosity and diffusion

Viscosity and tracer diffusion are implemented in the LOM in the following manner. First, parcel centers are partitioned into rows and columns that run parallel to each coordinate axis, where density is used for a vertical coordinate. Then each row or column of parcel centers is treated like a row or column of points in an Eulerian finite difference model. In other words, a flux of momentum or density is calculated between each parcel and its nearest neighbors in each mixing row or column in which it is contained. For more details on the implementation of vertical and horizontal diffusion, the reader is referred to Haertel et al. (2004, 2009), respectively.

f. Dividing and merging parcels

For computational efficiency, during the spinup simulation parcels are moved in groups of two and four in the middle (700–2100 m) and deep (>2100 m) ocean, respectively. This is essentially the same as using a lower vertical resolution in these regions. Because a single density is used for each group, the joining of parcels into a group creates

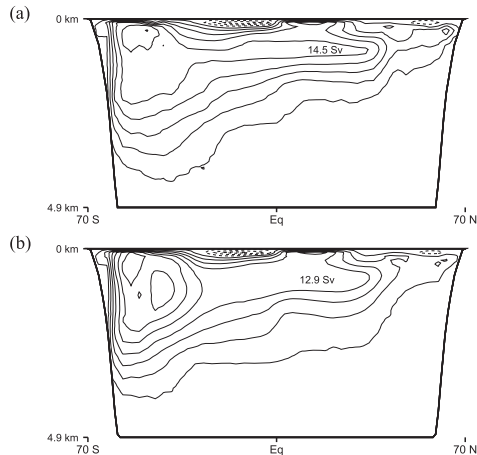


FIG. A3. Meridional overturning (contour interval 3 Sv) for simulations with higher resolutions: (a) double vertical resolution and (b) double horizontal resolution.

a small amount of tracer diffusion. However, only parcels in the same density class are joined, and after the spinup is complete the grouping of parcels is discontinued so that there is absolutely no tracer diffusion away from the surface. Moreover, the identities of individual parcels are maintained during the grouping so that individual parcels may be tracked through the merging and splitting process.

g. Sensitivity to model resolution

In order to test the sensitivity of our key results to model resolution we carried out two supplemental simulations that were initialized with the end state of the spinup simulation and were continued after parcels were divided either horizontally or vertically. These simulations were run for 300 years to allow the upper ocean to adjust to the new resolution. The upper-ocean density structure is surprisingly robust, changing very little when the vertical resolution is doubled or the horizontal resolution is doubled (not shown). The gross structure of the meridional overturning streamfunction is also the same for runs with higher horizontal and vertical resolution (Fig. A3). The deep cell is slightly more intense with a higher vertical resolution (Fig. A3a), and the Deacon cell is stronger with a higher horizontal resolution (Fig. A3b), presumably because of a stronger meander in the ACC (Fig. 13d).

The LOM has been developed over a number of years, and for more details on the numerical method, the mixing parameterizations, and tests that compare LOM simulations to analytic solutions and runs conducted with other ocean models the reader is referred to Haertel and Randall (2002) and Haertel et al. (2004, 2009). There are only a few differences between the model used here and that in Haertel et al. (2009): in this study, we use a Mercator projection, a modified leapfrog time differencing

with implicit treatment of Coriolis terms, and the modified form of gravity wave retardation described above, which has more straightforward energy conservation properties.

REFERENCES

- Barreiro, M., A. V. Fedorov, R. C. Pacanowski, and S. G. Philander, 2008: Abrupt climate changes: How the freshening of the northern Atlantic affects the thermohaline and wind-driven oceanic circulations. *Annu. Rev. Earth Planet. Sci.*, **36**, 33–58.
- Boccaletti, G., R. C. Pacanowski, S. G. H. Philander, and A. V. Fedorov, 2004: The thermal structure of the upper ocean. *J. Phys. Oceanogr.*, **34**, 888–902.
- , R. Ferrari, D. Ferreira, A. Adcroft, and J. Marshall, 2005: The vertical structure of the oceanic heat transport. *Geophys. Res. Lett.*, **32**, L10603, doi:10.1029/2005GL022474.
- Bryan, F., 1987: Parameter sensitivity of primitive equation ocean general circulation models. *J. Phys. Oceanogr.*, **17**, 970–985.
- Bryan, K., J. K. Dukowicz, and R. D. Smith, 1999: On the mixing coefficient in the parameterization of bolus velocity. *J. Phys. Oceanogr.*, **29**, 2442–2456.
- Bryden, H. L., and S. A. Cunningham, 2003: How wind forcing and air-sea heat exchange determine meridional temperature gradient and the stratification for the Antarctic Circumpolar Current. *J. Geophys. Res.*, **108**, 3275, doi:10.1029/2001JC001296.
- Cunningham, S. A., and Coauthors, 2007: Temporal variability of the Atlantic meridional overturning circulation at 26.5°N. *Science*, **317**, 935–938.
- Doos, K., and D. J. Webb, 1994: The Deacon cell and other meridional cells of the Southern Ocean. *J. Phys. Oceanogr.*, **24**, 429–442.
- , J. Nycander, and A. C. Coward, 2008: Lagrangian decomposition of the Deacon cell. *J. Geophys. Res.*, **113**, C07028, doi:10.1029/2007JC004351.
- Fedorov, A. V., R. C. Pacanowski, S. G. Philander, and G. Boccaletti, 2004: The effect of salinity on the wind-driven circulation and the thermal structure of the upper ocean. *J. Phys. Oceanogr.*, **34**, 1949–1966.
- , M. Barreiro, G. Boccaletti, R. Pacanowski, and S. G. Philander, 2007: The freshening of surface waters in high latitudes: Effects on the thermohaline and wind-driven circulations. *J. Phys. Oceanogr.*, **37**, 896–907.
- , C. Brierley, and K. Emanuel, 2010: Tropical cyclones and permanent El Niño in the early Pliocene epoch. *Nature*, **463**, 1066–1070.
- Ganachaud, A., and C. Wunsch, 1993: Large-scale ocean heat and freshwater transports during the World Ocean Circulation Experiment. *J. Climate*, **16**, 696–705.
- Gent, P. R., and J. C. McWilliams, 1990: Isopycnal mixing in ocean circulation models. *J. Phys. Oceanogr.*, **20**, 150–155.
- Gnanadesikan, A., 1999: A simple predictive model for the structure of the oceanic pycnocline. *Science*, **283**, 2077–2079.
- , and R. W. Hallberg, 2000: On the relationship of the Circumpolar Current to Southern Hemisphere winds in coarse-resolution ocean models. *J. Phys. Oceanogr.*, **30**, 2013–2034.
- Griffies, S. M., R. C. Pacanowski, and R. W. Hallberg, 2000: Spurious diapycnal mixing associated with advection in a z-coordinate ocean model. *Mon. Wea. Rev.*, **128**, 538–567.

- , and Coauthors, 2009: Coordinated ocean-ice reference experiments (COREs). *Ocean Modell.*, **26**, 1–46.
- Haertel, P. T., and D. A. Randall, 2002: Could a pile of slippery sacks behave like an ocean? *Mon. Wea. Rev.*, **130**, 2975–2988.
- , and K. Straub, 2010: Simulating convectively coupled Kelvin waves using Lagrangian overturning for a convective parameterization. *Quart. J. Roy. Meteor. Soc.*, **136**, 1598–1613.
- , D. A. Randall, and T. G. Jensen, 2004: Simulating upwelling in a large lake using slippery sacks. *Mon. Wea. Rev.*, **132**, 66–77.
- , L. Van Roekel, and T. Jensen, 2009: Constructing an idealized model of the North Atlantic Ocean using slippery sacks. *Ocean Modell.*, **27**, 143–159.
- Huang, R. X., 1988: On boundary value problems of the ideal-fluid thermocline. *J. Phys. Oceanogr.*, **18**, 619–641.
- , 1999: Mixing and energetics of the oceanic thermohaline circulation. *J. Phys. Oceanogr.*, **29**, 727–746.
- Iselin, C. O., 1939: The influence of vertical and lateral turbulence on the characteristics of the waters at mid-depths. *Trans. Amer. Geophys. Union*, **20**, 414–417.
- Ito, T., M. Woloszyn, and M. Mazloff, 2010: Anthropogenic carbon dioxide transport in the Southern Ocean driven by Ekman flow. *Nature*, **263**, 80–83.
- Jensen, T. G., 1996: Artificial retardation of barotropic waves in layered ocean models. *Mon. Wea. Rev.*, **124**, 1272–1283.
- Killworth, P. D., and C. W. Hughes, 2002: The Antarctic Circumpolar Current as a free equivalent-barotropic jet. *J. Mar. Res.*, **60**, 19–45.
- Kuhlbrodt, T., A. Griesel, M. Montoya, A. Levermann, M. Hofmann, and S. Rahmstorf, 2007: On the driving processes of the Atlantic meridional overturning circulation. *Rev. Geophys.*, **45**, RG2001, doi:10.1029/2004RG000166.
- Ledwell, J. R., A. J. Watson, and C. S. Law, 1993: Evidence for slow mixing across the pycnocline from an open-ocean tracer-release experiment. *Nature*, **364**, 701–703, doi:10.1038/364701a0.
- Luyten, J. R., J. Pedlosky, and H. Stommel, 1983: The ventilated thermocline. *J. Phys. Oceanogr.*, **13**, 292–309.
- Marshall, J., and T. Radko, 2003: Residual-mean solutions for the Antarctic Circumpolar Current and its associated overturning circulation. *J. Phys. Oceanogr.*, **33**, 2341–2354.
- Montgomery, R. B., 1938: Circulation in upper layers of southern North Atlantic deduced with the use of isentropic analysis. Massachusetts Institute of Technology Paper in Physical Oceanography and Meteorology, Vol. 6, No. 2, 55 pp.
- Nowlin, W. D., Jr., and J. M. Klinck, 1986: The physics of the Antarctic Circumpolar Current. *Rev. Geophys.*, **24**, 469–491, doi:10.1029/RG024i003p00469.
- Orsi, A. H., S. S. Jacobs, A. L. Gordon, and M. Visbeck, 2001: Cooling and ventilating the abyssal ocean. *Geophys. Res. Lett.*, **28**, 2923–2926.
- Park, Y.-G., and K. Bryan, 2000: Comparison of thermally driven circulations from a depth-coordinate model and an isopycnal-layer model. Part I: Scaling-law sensitivity to vertical diffusivity. *J. Phys. Oceanogr.*, **30**, 590–605.
- Pedlosky, J., 1996: *Ocean Circulation Theory*. Springer-Verlag, 450 pp.
- Polzin, K. L., J. M. Toole, J. R. Ledwell, and R. W. Schmitt, 1997: Spatial variability of turbulent mixing in the abyssal ocean. *Science*, **276**, 93–96, doi:10.1126/science.276.5309.93.
- Robinson, A. R. R., and H. Stommel, 1959: The ocean thermocline and associated thermohaline circulation. *Tellus*, **11**, 295–308.
- Rogerson, A. M., P. D. Miller, L. J. Pratt, and C. K. R. T. Jones, 1999: Lagrangian motion and fluid exchange in a barotropic meandering jet. *J. Phys. Oceanogr.*, **29**, 2635–2655.
- Saenko, O. A., 2007: Projected strengthening of the Southern Ocean winds: Some implications for the deep ocean circulation. *Ocean Circulation: Mechanisms and Impacts*, *Geophys. Monogr.*, Vol. 173, Amer. Geophys. Union, 365–382.
- Samelson, R. M., 2004: Simple mechanistic models of middepth meridional overturning. *J. Phys. Oceanogr.*, **34**, 2096–2103.
- , and G. K. Vallis, 1997: Large-scale circulation with small diapycnal diffusion: The two-thermocline limit. *J. Mar. Res.*, **55**, 223–275.
- Sevellec, F., and A. V. Fedorov, 2011: Stability of the Atlantic meridional overturning circulation and stratification in a zonally averaged ocean model: Effects of freshwater, Southern Ocean wind and diapycnal diffusion. *Deep-Sea Res. II*, **58**, 1927–1943, doi:10.1016/j.dsr2.2010.10.070.
- Talley, L. D., J. L. Reid, P. E. Robbins, 2003: Data-based meridional overturning streamfunctions for the global ocean. *J. Climate*, **16**, 3213–3226.
- Toggweiler, J. R., and B. Samuels, 1995: Effect of Drake Passage on the global thermohaline circulation. *Deep-Sea Res. I*, **42**, 477–500.
- , and —, 1998: On the ocean's large-scale circulation near the limit of no vertical mixing. *J. Phys. Oceanogr.*, **28**, 1832–1852.
- Tziperman, E., 1986: On the role of interior mixing and air-sea fluxes in determining the stratification and circulation of the oceans. *J. Phys. Oceanogr.*, **16**, 680–693.
- Vallis, G. K., 2000: Large-scale circulation and production of stratification: Effects of wind, geometry, and diffusion. *J. Phys. Oceanogr.*, **30**, 933–954.
- Van Roekel, L., T. Ito, P. Haertel, and D. Randall, 2009: Lagrangian analysis of the meridional overturning circulation in an idealized ocean basin. *J. Phys. Oceanogr.*, **39**, 2175–2193.
- Veronis, G., 1969: On theoretical models of the thermohaline circulation. *Deep-Sea Res.*, **16**, 301–323.
- Welander, P., 1959: An advective model of the ocean thermocline. *Tellus*, **11**, 309–318.
- Wolfe, C. L., and P. Cessi, 2009: Overturning in an eddy-resolving model: The effect of the pole-to-pole temperature gradient. *J. Phys. Oceanogr.*, **39**, 125–142.
- , and —, 2010: What sets the strength of the mid-depth stratification and overturning circulation in eddying ocean models? *J. Phys. Oceanogr.*, **40**, 1520–1538.
- Wunsch, C., and R. Ferrari, 2004: Vertical mixing, energy, and the general circulation of the oceans. *Annu. Rev. Fluid Mech.*, **36**, 281–314, doi:10.1146/annurev.fluid.36.050802.122121.
- Yuan, G.-C., L. J. Pratt, and C. K. R. T. Jones, 2004: Cross-jet Lagrangian transport and mixing in a 2½-layer model. *J. Phys. Oceanogr.*, **34**, 1991–2005.